Aberrant macrophage activation and failed regeneration of pulmonary epithelium promote tuberculosis progression uniquely in lung tissue

Running title:

Lung epithelium damage promote the aberrant macrophage activation in tuberculosis

Key words: tuberculosis, lung, macrophage, immunity, epithelium, interferon

Authors and Affiliations

Shivraj M. Yabaji[1]

Ming Lo[1]

Suruchi Lata[1]

Igor Gavrish[1]

Anna E. Tseng[1]

Aoife K O'Connell[1]

Hans P Gertje[1]

Sarah Mazzilli[4]

Shumin Tan[7]

Colleen E Thurman[1]

William R Bishai[5]

Nicholas Crossland[1,3]

Lester Kobzik[6]

Igor Kramnik[1,2,8]

Affiliations

1. The National Emerging Infectious Diseases Laboratories (NEIDL), Boston University, Boston, MA 02118.

2. Pulmonary Center, The Department of Medicine, Boston University Chobanian & Aveedisian School of Medicine, Boston, MA 02118.

3. The Department of Pathology and Laboratory Medicine, Boston University Chobanian & Avedisian School of Medicine, Boston, MA 02118

4. Division of Computational Biomedicine, Boston University Chobanian & Avedisian School of Medicine, Boston, MA 02118.

5. Center for Tuberculosis Research School of Medicine, John Hopkins University, Baltimore, Maryland

6. Cellecta, Inc., Mountain View, CA

7. Department of Molecular Biology and Microbiology, Tufts University School of Medicine, Boston, MA

8. Corresponding author: ikramnik@bu.edu

Abstract

Pulmonary TB that develops in immunocompetent adult humans is responsible for approximately 85% of the disease burden and is central for Mtb transmission. Most humans contain Mtb infection within primary granulomatous lesions, but in certain immunocompetent humans, containment fails, leading to hematogenous spread and active pulmonary disease with the formation of necrotic lesions and cavities that enable Mtb transmission via aerosols. To reveal lung-specific microenvironments conducive for Mtb survival and replication despite systemic immunity, we use fluorescence multiplex immunohistochemistry and spatial transcriptomic analyses of heterogenous TB lesions that uniquely form in the lungs of immunocompetent but TB-susceptible B6.Sst1S mice after hematogenous spread from the primary lesion. Initially, these secondary lung lesions manifested local adoptive immunity featuring tertiary lymphoid follicles similar to resistant B6 mice and contained primarily non-replicating bacilli. Following these early events, however, the B6.Sst1S mice uniquely demonstrate expansion of myeloid cell populations with the appearance of alternatively activated macrophages, dissolution of lymphoid follicles, and the accumulation of de-differentiated lung epithelial cells. These processes led to bronchogenic expansion, broncho-occlusion, and necrosuppurative pneumonia closely resembling advanced pulmonary tuberculosis in humans. To determine whether lung parenchymal cells or lung oxygenation were necessary for the pulmonary TB progression, we implanted lung and spleen fragments subcutaneously prior to the infection. The lung implants uniquely displayed the formation of the characteristic organized granulomas with necrosis and Mtb replication that paralleled TB progression in native lungs, demonstrating that the cellular composition of inflamed lung tissue, not oxygenation, is a critical determinant of pulmonary TB progression. Our data demonstrate that deleterious bi-directional interactions of aberrantly activated macrophages with the inflammation-injured lung resident cells determine lung vulnerability to virulent Mtb in immunocompetent hosts. Because these mechanisms enable Mtb transmission among humans

via aerosols, they are likely evolutionary conserved and, therefore, represent appealing targets for host-directed TB therapies.

Introduction

Tuberculosis remains a top global health problem. It is estimated that ~25% of all people have been infected with *Mycobacterium tuberculosis* (Mtb)(*1*). The majority of immunocompetent humans, however, restrict primary TB infection and remain latently infected and non-infectious. However, approximately 5-10% of the latently Mtb-infected people can later develop active TB disease during their lifetime. Pulmonary TB is the major clinical form of TB that accounts for approximately 85% of all TB cases representing the major causes of TB morbidity and mortality(*1-3*). This clinical form of TB mostly develops in immunocompetent adult humans despite prominent Mtb-specific immune responses, and it is not efficiently prevented by BCG immunization(*1, 4, 5*).

Mtb is a specialized human pathogen that does not have natural reservoirs, and its co-evolution with natural human hosts is entirely dependent on human-to-human transmission (*6*). The unique vulnerability of the human lung to TB is crucial for Mtb transmission via aerosols - the only epidemiologically significant route in human populations. Lung tissue serves as a gateway for Mtb infection, where finely aerosolized Mtb particles reach alveoli to infect alveolar macrophages and induce the formation of primary TB lesions. These lesions are often sufficient to contain the infection and “arrest” the bacterial spread without complete eradication, thus setting a stage for subsequent TB progression, when conditions permit. The formation of cavitary pulmonary TB formation is an end stage of Mtb life cycle within the host that is required for the production of infectious aerosols and Mtb transmission(*5*). In endemic areas primary infection with Mtb usually occurs in childhood, while the development of the most infectious form - pulmonary TB with cavitary lesions - occurs in immunocompetent adults, despite pre-existing immunity and previous Mtb containment.

Current evidence suggests that pulmonary TB in previously infected individuals may develop after respiratory re-infection(*7, 8*) or as shown in classic studies after seeding the lungs following hematogenous spread (reviewed in(*2, 5, 9*)). After respiratory infection, TB lesions

may develop in internal organs other than respiratory tract, most notably in the brain, bones, kidney and adrenals, thus demonstrating the hematogenous spread of the bacteria from the primary site of infection. In animal models, the bacterial dissemination occurs during the initial weeks after the aerosol infection(*10-12*). In humans, there is also a stage of detectable Mtb bacteremia(*13*) that may occur within weeks after primary infection, during which bacilli disseminate from the primary lesion and may implant in any organ including the opportunity to re-seed the lungs. Alternatively, the bacterial dissemination may occur from recrudescent primary lesions after a period of latent TB infection (LTBI). In both cases, the bacteria seeds the lung tissue and induce the *de novo* secondary lesions at the sites distant from the primary lesions, as evidenced by the simultaneous presence of the active TB lesions, often found in lung apices, and calcified inactive primary lesions elsewhere in the lungs(*14*). The secondary lesions develop in hosts with activated adaptive immunity to Mtb that initially help contain their progression(*15*). However in the lungs, most often in the apical regions distinct from the location of primary lesions, the secondary lesions may eventually progress and undergo necrotization to form aerated cavities – a protected niche for the bacterial proliferation and subsequent aerosol transmission.

Classic TB treatises(*2*) and recent studies by Hunter and colleagues emphasize the pathomorphological distinctions between primary and secondary, or post-primary, pulmonary TB lesions in human patients(*14, 16, 17*). The primary TB lesions develop in the lungs after direct aerosol deposition of single Mtb bacteria into intact alveoli. They are represented by organized TB granulomas with characteristic central necrosis surrounded by concentric layers of immune cells and fibrotic tissue. In contrast, the pulmonary TB lesions that develop after the hematogenous Mtb spread morphologically represent areas of granulomatous pneumonia that undergo necrotization leading to massive lung tissue damage with the formation of aerated cavities (reviewed in(*12, 17, 18*)). In the immunocompetent hosts, these lesions are walled off by inflammatory tissue from the intact lung and facilitate Mtb transmission by allowing highly

infectious individuals remain active despite extensive local lung damage before they are diagnosed or succumb to infection(*19, 20*).

An improved understanding of the mechanisms behind failed TB containment uniquely in the lungs of immunocompetent individuals would enable interventions to control the pulmonary TB progression and transmission among natural human hosts. However, despite the predominance of post-primary pulmonary TB among human TB patients, its evolutionary significance and recognition as a distinct clinicopathologic entity by human pathologists, its mechanisms are much less understood and studied as compared to primary TB.

A central mechanistic question is what happens in the 5-10% of humans with latent TB infection (LTBI) that eventually progress to clinical pulmonary TB(*19*). The importance of studying mechanisms of pulmonary TB that develops despite pre-existing systemic immunity, either after primary infection or immunization, are comprehensively discussed in a recent review(*4*). Of particular practical importance is understanding why BCG vaccination protects against disseminated TB but does not offer equal protection from pulmonary TB. While a delay in T cell activation explains the initial bacterial advantage after primary airborne infection, the pulmonary TB after re-activation or re-infection occurs in individuals with pre-existing immunity. An inadequate T cell recruitment and/or access to the sites of infection was proposed to explain failures of T cell-mediated immunity in the lung lesions (reviewed in(*4, 21-24*)). Alternatively, the detrimental effect of immune activation, initially described as the Koch phenomenon, is regarded as a plausible mechanism of pulmonary tissue damage impeding the development of safe immunotherapy for TB disease(*18, 25, 26*). Along these lines, it has been proposed that evolutionary conserved Mtb antigens induce T cell-mediated lung damage to facilitate Mtb transmission(*27, 28*).

Among non-immunological mechanisms of the lung vulnerability to TB, the aeration of lung tissue has been considered as a likely mechanism of Mtb lung tropism after hematogenous spread, because in vitro the bacteria replicate faster in aerated cultures. Several studies also

suggest the possible involvement of lung epithelium and fibroblasts and mesenchymal cells in the formation of primary TB lesions(*29-31*). In addition, Ernst and colleagues revealed a previously unsuspected role for IFNγ in nonhematopoietic lung cells in the regulation of lung pathology at later stages of the disease(*32*).

As in humans, lung tissue in mammals is also particularly vulnerable to TB progression irrespective of a route of infection(*10, 12*). Summarizing many independent mouse studies, Robert North postulated that the murine model was particularly suitable for the mechanistic dissection of the lung vulnerability(*11*). For example, in immunocompetent inbred mice, pulmonary TB develops after a primary systemic intravenous infection. Although only 0.1% of the inoculum is initially distributed to the lungs, within a month after infection the bacterial loads in the lungs are orders of magnitude higher than at the sites of the initial Mtb deposition in the spleen and liver. This lung specificity is lost in immunodeficient *scid* mice, where fulminant TB growth leads to disorganized necrotic inflammation in other organs as well(*33*). These observations suggest that Mtb-specific adaptive immunity is necessary for systemic Mtb control, but it is less efficient in the lungs.

Currently, most animal TB models including the mouse model introduce Mtb directly into the lung by aerosol infection or intratracheal instillation, thus recapitulating the primary TB. Recognizing the need for animal models recapitulating pulmonary TB progression after hematogeneous spread both for the mechanistic studies and for testing specific interventions, a mouse TB model has been tested where primary TB lesions were induced through intradermal Mtb infection(*34*). However, in the common inbred mouse strain genetically resistant to virulent Mtb, C57BL/6J, the intradermal Mtb infection induced T cell-mediated immunity and protection against subsequent aerosol challenge(*35*). In this model, pulmonary TB developed only after suppression of essential mechanisms of anti-tuberculosis immunity, such as depletion of NO, neutralization of IFNγ, or CD4+ T cell depletion(*36, 37*).

Here, we describe the progression of human-like pulmonary TB lesions after subcutaneous infection in immunocompetent but susceptible to TB mice that carry the susceptibility allele at the *sst1* (*supersusceptibility to tuberculosis* 1) locus(*38, 39*). Previously, we found that the *sst1* susceptibility allele was specifically responsible for massive lung necrosis after intravenous infection and for the formation of chronic necrotic TB granulomas after a low dose aerosol infection. In the latter model, the B6.Sst1S mice initially controlled the infection similarly to the resistant B6 wild type mice, but they developed organized necrotic granulomas after 2-3 months(*39*). In both models, the *sst1*-mediated susceptibility was lung-specific and clearly distinct from acute TB with necrotic lung inflammation observed in mutant mice with inactivation of essential mechanisms of anti-tuberculosis immunity, such as *scid,* and the knockouts of iNOS or the receptors of IFN-gamma, TNF and IL-1(*33*). Thus, the *sst1* locus does not confer systemic immunodeficiency and, similar to non-human primates and humans, the progression of pulmonary TB in B6.Sst1S mice proceeds despite the activation of innate and adaptive immunity, which is sufficient for the systemic control of infection.

Using reciprocal bone marrow chimeras, we found that the *sst1*-mediated phenotype was expressed by the bone marrow-derived myeloid cells(*40*). In vitro, the bone marrow-derived macrophages homozygous for the *sst1* susceptibility allele displayed an aberrant activation pattern characterized by reduced control of intracellular bacteria, unresolving stress and the hyperactivity of type I interferon (IFN-I) pathway(*41*). Although these findings might predict widespread infection in multiple organs, the phenotypic expression of the *sst1* susceptibility allele in vivo occurred uniquely within the lung environment. In bone marrow chimeras the lung-specific progression partitioned with the *sst1* susceptibility alleles of the bone marrow donor but was independent of the recipient *sst1* genotype. Moreover, BCG vaccination or adoptive transfer of T lymphocytes from the vaccinated mice delayed but did not prevent the formation of the necrotic TB lesions in the lungs of the *sst1*-susceptible mice(*33*). These studies demonstrated that the aberrant macrophage activation limited the efficiency of T cell-mediated

immunity specifically within the lung lesions and allowed progression of pulmonary TB even in the presence of pre-existing immunity.

In this study, we characterized pulmonary TB lesions that develop after hematogenous spread from remote primary lesions in both the resistant wild type C57BL/6 (B6) and *sst1* susceptible congenic B6.Sst1S mice. While the dissemination and the formation of early interstitial pulmonary microlesions occurred in both strains, only in the *sst1* susceptible mice pulmonary lesions uniquely advanced to necrosuppurative pneumonia that resemble massive lung tissue damage preceding the formation of lung cavities in humans. Subsequent mechanistic dissection revealed important contributions of lung epithelial cells and macrophage polarization to the lesion progression towards the human-like pulmonary TB.

Results

I. Pulmonary TB progression in *sst1*-susceptible mice after dissemination from a distant site of infection

To ensure that pulmonary TB lesions develop after initial priming of adaptive immunity and hematogenous spread, we infected B6.Sst1S mice with virulent Mtb suspension subcutaneously (SQ) overlying the hock, an established alternative to footpad injection(*42*). We have chosen the SQ hock infection to model the hematogenous TB spread, because 1) it allows clear separation of the primary site of infection from secondary, metastatic, lesions; 2) the only anatomically possible route of lung colonization is through hematogenous dissemination, resembling reactivation TB progression in humans; 3) SQ hock injection is a common route of immunization(*42*), and T cell-mediated immunity is rapidly induced in the regional (popliteal) lymph node after subcutaneous and intradermal immunizations(*35, 43*). In our pilot experiments, we determined that hock infection in adult female mice with 10^6 CFU of Mtb Erdman resulted in

the formation of pulmonary granulomatous lesions in 100% of the animals by 12 wpi (**Suppl. Table 1**). The disease progression was similar in males and female mice (**Suppl. Table 2**).

At 6 weeks post infection (wpi), the bacteria were found in moderately enlarged regional (popliteal) lymph nodes on the ipsilateral side of infection. There, the bacteria localized intracellularly within small macrophage aggregates, did not extensively replicate, and did not cause the formation of necrotic granulomas (**Fig.1A**). Lung lesions could also be detected at 6 – 12 wpi. At 12 wpi we found heterogeneous lung lesions. Small, mostly interstitial, lesions were composed of lymphocytes and macrophages with notable absence of granulocytes and contained very few bacteria (**Fig.1B**).

The intermediate lesions were enlarged and contained an increased proportion of myeloid cells consisting primarily of epithelioid macrophages (**Fig.1C**). In some lesions we observed the presence of cholesterol clefts, suggesting cell death, with minimal single cell necrosis and/or neutrophil influx. At this stage the bacterial population moderately increased in size, yet remained intracellular, and only a small proportion of macrophages were infected. The bacteria were found mostly as sparse single bacilli or intracellular clusters suggestive of moderate intracellular replication.

The advanced B6.Sst1S lesions contained clusters of replicating Mtb located intra- and extracellularly and areas of marked to severe granulomatous interstitial pneumonia characterized by interstitial and alveolar accumulation of epithelioid macrophages mixed with occasional multinucleated giant cells, frequent cholesterol clefts, mild to moderate amounts of karyorrhectic debris (lytic necrosis) and frequent neutrophilic infiltrates **(Fig.1D)**. Yet, reactive epithelioid macrophages cells remained the most numerous cell population in these lesions.

Intriguingly, a subset of B6.Sst1.S infected mice (five of twenty-nine animals examined) develop a distinct, severe, necrosuppurative pneumonia phenotype between 11 and 20 weeks post infection. Necrosuppurative pneumonia always affected more than 50% of the total pulmonary parenchyma (**Fig.2C, Suppl.Fig.1A**) and was characterized by loss of normal

pulmonary parenchymal architecture that was replaced by large amounts of eosinophilic, granular to amorphous, acellular material (necrosis), innumerable degenerative neutrophils and macrophages, admixed with large amounts of karyorrhectic debris (**Suppl.Fig.1B, 1D, and 1E**). The degenerate leukocytes and necrotic debris extended into the lumen of multiple bronchioles causing their occlusion (**Suppl.Fig.1G**). Occasional small amounts of basophilic, amorphous material (dystrophic mineralization) were scattered within necrotic areas (**Suppl.Fig.1E**). Fibrinoid necrosis and fibrin thrombi were occasionally observed in medium to large-caliber vessels in the affected pulmonary parenchyma (**Suppl.Fig.1H**). The heaviest acid-fast bacilli load (++++) was consistently observed in animals with the necrosuppurative pneumonia phenotype, and both intracellular and extracellular acid-fast bacilli were observed (**Suppl.Fig.1C, 1F, 1I and Suppl. Table 3**). These experiments demonstrated Mtb dissemination to the lung and subsequent lesion progression towards severe necrotizing pneumonia in B6.Sst1S mice.

II. The *sst1* locus drives pulmonary TB progression.

To assess specific effects of the *sst1* locus on pulmonary TB after SQ hock infection, we compared the disease progression in the wild type B6 and congenic B6.Sst1S mice. The B6.Sst1S mice were significantly more susceptible, as evidenced by their lower weight and decreased survival (**Fig.2A and B**). During the 20 wpi period of observation about 35% of B6.Sst1S mice reached the terminal stage featuring marked weight loss, respiratory distress and rapid deterioration of clinical status that required euthanasia. The lungs lesions of these animals were represented by either severe granulomatous interstitial pneumonia or coalescing necrosuppurative pneumonia as described above.

In the surviving animals, pulmonary TB lesions were found in both resistant (B6) and susceptible (B6.Sst1S) animals at 11 and 20 wpi. Quantitative analysis of pulmonary

inflammation and Mtb loads of lung lesions demonstrated overall increased inflammation and marked heterogeneity of the B6.Sst1S lung lesions at both timepoints (**Fig.2C** and **Suppl.Fig.2**). Based on semi-quantitative assessment of acid fast Mtb loads (**Suppl.Fig.2B** and **Suppl. Table 3**), the B6.Sst1S lung lesions were divided into 3 categories with high, intermediate, and low bacterial loads (**Fig.2D**). In these animals, the bacteria could also be found in the spleen, popliteal lymph node, liver, and gut-associated lymphoid tissue (**Suppl. Tables 4 and 5**). In these organs, however, Mtb localized exclusively within small macrophage aggregates with no evidence of extensive bacterial replication, neutrophil influx, or necrosis (**Suppl.Fig.3**). Comparisons of the organ loads (represented by colored dots for each assessed organ) in individual animals (X axis), demonstrated substantially higher bacterial loads in the advanced and intermediate lung lesions as compared to other organs of the same animal (**Fig.2D**).

Interestingly, the pulmonary lesions were also found in B6 mice at both 11 and 20 wpi (**Fig.2D-E**). At both timepoints, the majority of C57BL/6J infected animals had minimal to mild granulomatous interstitial pneumonia similar to the B6.Sst1S lesions with no detectable to low Mtb load (**Fig.2D, Suppl. Table 3**). These insipient microscopic lesions developed interstitially in the vicinity of blood vessels and featured prominent lymphoid follicles containing lymphoplasmacytic infiltrates (**Fig.2F,** upper panels and **Suppl.Fig.4A**). To further compare the pulmonary lesion composition, we employed fluorescent multiplexed immunohistochemistry (fmIHC) using myeloid markers Iba1, iNOS, and Arg1, and CD3ε and CD19 for the detection of T and B lymphocytes, respectively. The early lesions in both backgrounds prominently featured organized CD19+ B cell follicles and numerous CD3ε+ T cells. The myeloid compartment was represented by Iba1+ macrophages, a fraction of which was activated as evidenced by iNOS+ expression (**Fig.2F, middle and lower panels,** and **Suppl.Fig.4B**). Sparse individual bacteria localized exclusively inside macrophages (**Suppl.Fig.2B**), and the vast majority of iNOS+ activated macrophages contained no acid fast bacilli. These data demonstrate that the initial TB

lesions in the lungs were represented by active adaptive and innate immune responses sufficient for bacterial containment, but seemingly disproportionate to the bacterial loads.

To exclude a possibility that lesion formation was driven by non-acid-fast forms of Mtb, we combined acid fast staining with IHC using polyclonal anti-mycobacterial antibodies – both methods produced an overlapping pattern confirming that the incipient lesions contained relatively few infected macrophages (**Suppl.Fig.5A,** left panel). To further confirm this observation, we infected mice with Mtb Erdman expressing constitutive fluorescent reporter mCherry and a replication reporter(*44*). To survey greater portion of the inflammatory lung tissue, we imaged the reporter bacteria in 50 – 100 μm thick sections using confocal microscopy after tissue clearing. This method also demonstrated that the intracellular bacteria in the early lesions were mostly represented by single or, rarely, double bacilli, per macrophage with little replication (**Suppl.Fig.5B**).

Thus, the initial organization of the TB lesions involved major branches of the innate and adaptive immunity. It was triggered in both genetic backgrounds by few persisting bacteria and was most likely driven by secreted Mtb products or/and inflammatory mediators. Thus, the extensive local reaction did not reflect, but preceded, the bacterial growth.

Further progression of pulmonary TB lesions within the 24 wpi observation period was evident only in B6.Sst1S mice. Initially, it was characterized by an increase in bacterial loads, the fraction of infected macrophages, the number of intracellular bacilli and clustering of Mtb bacilli inside infected macrophages (**Fig.2D**, **Suppl.Fig.2B**). The fraction of replication reporter positive Mtb in these lesions increased to approximately 50%, as compared to the few replication-positive Mtb in the incipient lesions (**Suppl.Fig.5B,** left and middle panels), indicating the local macrophage failure to control the bacterial growth. Therefore, for further analyses of pulmonary TB progression, we classified the lung lesions based on the bacterial loads as controlling (C) and non-controlling (NC) (**Fig.2G**). Of note, the latter category did not include the

advanced necrotizing (**Fig.1D**) and terminal necrotic lesions (**Suppl.Fig.1, Suppl.2B** (4+), **Suppl.Fig.5B,** right panel).

To quantitatively compare the myeloid and lymphoid cell populations within C vs NC lesions, we utilized fmIHC and a random forest Tissue Classifier (TC) for automated identification and annotation of granulomatous lesions. In particular, positive pixel area quantification analysis to quantify myeloid populations and high-plex immunophenotyping for quantifying lymphoid density using Halo image analysis software were performed (**Fig.2I**). The proportion of myeloid and lymphoid populations were similar in the controlling lesions of B6 and B6.Sst1S. Compared to C lesions, the NC lesions of B6.Sst1S mice exhibited disorganized B cell follicles, scattered B cells, and more numerous T cells. Although the total population of non-activated (Iba1+iNOS-Arg1-) macrophages were similar in both lesions, the proportion of activated M1 macrophages (iNOS+) was greater in NC lesions (**Fig.2G, I and Suppl.Fig.4B**). The excess of activated macrophages (iNOS+) in NC lesions was confirmed using confocal microscopy of thick sections that also demonstrated that the majority of iNOS+ cells were uninfected, but adjacent to the infected cells (**Fig.2H**). Some NC lesions also contained Arg1+ cells, although their proportion was approximately 10-fold lower as compared to the iNOS+ macrophages (**Fig.2I**). Thus, the NC lesions represented increased inflammation featuring disorganization of B cell follicles, an increased proportion of iNOS+ activated macrophages and the concomitant appearance of alternatively activated Arg1+ macrophages.

Taken together, these data demonstrate: (i) the hematogenous spread of Mtb to many organs after SQ hock infection; (ii) the initial immune-mediated control of Mtb and persistence in multiple organs, including the incipient TB lesions in the lungs; (iii) progression of the lesions specifically in the lungs of B6.Sst1S mice that range from granulomatous inflammation to lethal necrosuppurative pneumonia. The initial lesion progression in the *sst1*-susceptible mice was associated with the loss of organized lymphoid tissue, an expansion of the activated macrophage populations and gradual increase of the intracellular pool of replicating bacilli.

III. Effect of genetic background on TB progression in *sst1* susceptible mice.

To test the effects of the host genetic background on the TB progression in *sst1*-susceptible mice, we compared two *sst1*-susceptible inbred mouse strains: B6.Sst1S, the commonly used C3HeB/FeJ(HeB), and their hybrids (HeB x B6.Sst1S)F1. By 14 wpi, all the mice developed pulmonary TB lesions. According to the survival, weight and Mtb organ loads and lesion morphology, the B6.Sst1S mice were the most susceptible (**Suppl.Fig.6** and **Suppl. Table 6**). Several B6.Sst1S lesions contained replicating bacilli, areas of micronecrosis with neutrophil infiltration, while the pulmonary TB lesions of (HeB x B6.Sst1S)F1 hybrid mice contained fewer replicating bacteria and no necrosis (**Fig.3A**). Therefore, these lung lesions were classified as non-controlling advanced (NC-A) and non-controlling intermediate (NC-I), respectively.

To identify pathways associated with the NC-I-to-NC-A progression, we compared representative (HeB x B6.Sst1S)F1 (NC-I) and B6.Sst1S (NC-A) lesions using Nanostring GeoMx Digital Spatial Profiler (DSP) spatial transcriptomic platform. Regions of interest (ROI) were selected to focus on myeloid-rich areas avoiding necrosis and tertiary lymphoid tissue, with uninvolved (U) lung areas serving as controls. A total of eight areas of each (uninvolved lung, NC-I and NC-A lesions) were selected and analyzed using the Mouse Whole Transcriptome Atlas (WTA) panel which targets 21,000+ transcripts for mouse protein coding genes. The analysis identified 793 differentially expressed genes (DEG) with $q \leq 0.05$ (**Suppl. Table 7**). Both Principal Component Analyses (PCA) and hierarchical clustering demonstrated remarkable concordance within the groups and consistent differences between the groups (**Fig.3B**).

For digital deconvolution of the cellular content of the ROIs we used CIBERSORTx software (**Fig.3D**). It demonstrated the decreased T and B lymphocyte content, the increased

proportions of macrophages and neutrophils, and a notable decline in monocyte to macrophage ratio in the NC-A lesions. These computational predictions were consistent with fmIHC data (**Fig.3A** and **C** and **Suppl.Fig7A**).

Using the DEG sets we performed Gene Set Enrichment Analysis (GSEA)(*45*). The top 10 pathways differentiating the NC-I and NC-A (non-controlling Intermediate and Advanced) lesions are listed in **Suppl. Table 8**. Among them, the upregulation of genes in inflammatory pathways, TNF and IL-6 signaling, and complement pathways were consistent with increased macrophage activation. An increased hypoxia pathway activation was consistent with increased size of the NC-A lesions and intravascular thrombosis. Confirming the escalating hypoxia, the accumulation and nuclear translocation of HIF1α significantly increased within the NC-A lesions (**Fig.3E** and **Suppl.Fig.7B**).

Comparing the DEG gene lists upregulated in NC-A vs NC-I lesions, we also observed the upregulation of known pathway markers, such as type I interferon (IFN-I) stimulated genes (Acod1, Rsad2, Il1rn, Ifitm6, Slnf4, Slfn8), metalloproteases (Mmp3, Mmp8, Mmp9, Mmp12, Mmp13, Adam8, Adamts4), oxidative stress (Hmox1) and proteotoxic stress (Hspa1a), and survival (Ier3). The neutrophil-related genes were represented by neutrophil chemoattractants (Cxcl1, Cxcl2, Cxcl3, Cxcl5, IL-17, IL36g), neutrophil growth factor (CSF3/G-CSF) and neutrophil proteins (S100a8 and S100a9, CD177, Lcn2, Lrg1).

Unexpectedly, we observed a coordinated upregulation of markers of M2 macrophage polarization (Arg1, Arg2, Fizz1/resistin-like beta/gamma, Chil1, CD300lf). Indeed, fmIHC confirmed the appearance of a significant population of Arg1+ macrophages (concurrently Iba1+) in the NC-A lesions (**Fig.3C, 3F** and **Suppl.Fig.7A**). Of note, the Arg1+ and iNOS+ macrophage populations were distinct, as clearly shown by spatial analysis using HALO (**Fig.3G**). Interestingly, these macrophage populations were mostly juxtaposed, resembling cloaking of the iNOS+ macrophages by the Arg1+ macrophages (**Fig.3H** and **Suppl.Fig.7C**). In

agreement with the upregulation of fibrosis markers (tgfbi and Col5a3), we demonstrated increased collagen deposition using Mason's trichrome staining.

Thus, DSP and IHC analyses of the pulmonary TB progression in susceptible hosts demonstrated a coordinated transition from lymphocyte-dominated to a myeloid-dominated inflammatory lesions, their functional transformation characterized by the appearance of alternatively activated macrophages, neutrophils, tissue damage and extracellular matrix remodeling.

IV. Reactions of lung epithelial cells embedded within TB progression

Among the top 10 pathways upregulated in the advanced lesions were epithelial pathways - Epithelial-Mesenchimal Transition (EMT) and K-RAS signaling, suggesting perturbations of lung epithelial cells within the TB lesions. Indeed, prominent cytokeratin-positive epithelial cell clusters were present within the ROIs (**Fig.4A**). We characterized these cells using alveolar pneumocyte markers: Caveolin 1 (Cav1), NK2 homeobox 1 (Nkx-2.1/ Ttf1) and pro-surfactant protein C (Pro-SpC). The uninvolved lung tissue contained the squamous Cav1+ Type I pneumocytes (AT1 cells) that lined the alveolar surface, while the cuboidal Ttf1+Pro-SpC+ cells represented typical Type II pneumocyte (AT2 cells) morphology, which are more sparsely distributed within alveoli. Within the lung TB lesions, Cav1+ cells were found embedded within the lesions clearly recapitulating the shape of the alveolar network (**Fig.4B** and **Suppl.Fig.8**). In contrast, the Ttf1+ cells within TB lesions often clustered together (**Suppl.Fig.9A**). Notably, a large fraction of Ttf1+ cells within TB lesions did not co-express the differentiation marker of AT2 cells (pro-SpC) (**Fig.4B**) and their proportions tended to be higher in more advanced lesions (**Fig.4C**). These clusters of Ttf1+ Sfptc- cells resemble the expansion of lineage-negative precursors (LNEP) that help repair alveolar lining after extensive chemical injury(*46*). Using staining for cytokeratin 6 we revealed the presence of abnormal epithelial cell

clusters within dysorganized non-controlling lesions of B6.Sst1S mice that was not observed in normal neighboring alveolar parenchyma or in B6 mice at 20 WPI (**Suppl.Fig.9B**). These data suggest that within the pulmonary TB lesions alveolar pneumocytes are intricately affiliated with the immune cells and undergo transition to an aberrant repair phenotype in parallel with the lesion progression.

Recently a subpopulation of lung precursors induced by chemical injury was found to express the IFN-I signature(*47*). Given the importance of the IFN-I pathway in TB susceptibility in mice and human patients(*48*), we used a B6.Sst1S,*ifnb*-YFP reporter mouse strain to test whether Tf1+ cells express IFNβ within TB lesions. The majority of YFP+ (IFNβ expressing) cells within TB lesions were iNOS+ activated macrophages. Additional cell types determined to express the IFNβ reporter YFP included Iba-1+- perivascular mononuclear cells, and bronchiolar epithelium in close proximity to granulomatous lesions (**Fig.4D, Suppl.Fig.10A**). The YFP+Ttf1+ cells were also clearly detectable. In these cells, YFP expression was observed exclusively in Ttf1+Pro-Spc- undifferentiated cells (**Fig.4D**).

To further characterize the YFP-expressing cells in TB lesions of the Mtb-infected B6.Sst1S,*ifnb*-YFP mice, we used 3D imaging of cleared thick sections. First, we confirmed the presence of Ttf1+YFP+ cells (**Fig.4E**). We also noted that highly YFP-positive cells were not uniformly spread within the lesions, but colocalized with residual alveolar arches (**Suppl.Fig.10B**). We used co-staining with epithelial marker pancytokeratin (panCK, **Suppl.Fig.10C**) and fibroblast marker smooth muscle actin (αSMA, **Suppl.Fig.10D**) to determine whether these YFP-expressing cells were of epithelial or fibroblast origins. However, fmIHC and 3D imaging clearly demonstrated that the high levels of YFP expression was not associated with these cell types but was associated with macrophages adjacent to the residual lung structures embedded within the lesions. Thus, alveolar cells not only survive within TB

lesions, but undergo transformation resembling damage-associated regeneration and their proximity may influence activation of adjacent inflammatory cells, such as macrophages.

To characterize functional states of lung epithelial cells embedded within TB lesions we used GeoMx DSP spatial transcriptomic analysis of pan-cytokeratin positive (panCK+) cells within the NC-A and NC-I TB lesions and compared them to the uninvolved lung (U) (**Fig.5A and Suppl. Table 9**). Pathways overexpressed in both NC-A and NC-I lesions as compared to U were 1) cytokine responses: Interferon type I and type II, TNFa, and IL6/STAT3; 2) cell growth and differentiation: mTORC1, K-Ras signaling, apical junction and Epithelial-Mesenchymal Transition (EMT); 3) metabolism: hypoxia, angiogenesis and glycolysis; 4) stress responses: p53 and UV responses, reactive oxygen species, xenobiotic metabolism, and apoptosis pathways (**Fig.5B** and **Suppl. Table 9**). These data illustrate that intralesional epithelial cells sense and respond to inflammatory cytokines produced by the adjacent activated macrophages, experience stress and hypoxia, and change their differentiation pattern. Comparing the epithelial transcriptomes of panCK+ cells in NC-A vs NC-I lesions, i.e. during TB progression, we noted the escalation of the same inflammatory, stress and hypoxia pathways (**Suppl. Table 9**).

To search for factors secreted by epithelial cells that might contribute to the disease progression, we compiled a custom list of secreted proteins and receptors, including genes expressed by lung epithelial cells during the immune response to mycobacteria(*30*) or in cross-talk with lung macrophages(*49*). Filtering the DEGs identified in CK+ cells with this list showed that the advanced lesions expressed higher levels of numerous relevant mediators, e.g. chemoattractants: chemokines Ccl3, Ccl20, CXCL10, IL17, immunosuppressant Il1rn (IL1 receptor antagonist), and developmental regulators Jag2 (canonical Notch ligand), Csf1 (M-CSF) and Csf3 (G-CSF) (**Fig.5C**).

Besides its canonical role in myelopoiesis, CSF1 produced by tumor cells was shown to play an important role in creating an immunosuppressive microenvironment by inducing tumor

associated macrophages (TAMs)(*50, 51*) and causing CNS injury in multiple sclerosis(*52*) and Alzheimer-like pathology(*53*). Besides, it has been involved in M2 macrophage polarization(*54*). We hypothesized that CSF1 produced by epithelial cells within TB lesions may exacerbate inflammation and inhibit Mtb control by macrophages. Therefore, we tested the effects of CSF1R inhibitors on control of Mtb replication by bone marrow-derived macrophages (BMDMs) grown in the presence of CSF1. First, we confirmed that CSF1 receptor (CSF1R) specific inhibitors (BLZ945 and PLX3397) induced BMDM cell death in our model (similar to CSF1 deprivation) (**Suppl.Fig.11A, B, D and E**). Then, we treated B6.Sst1S BMDMs with sublethal inhibitor concentrations before and during the course of infection with virulent Mtb. At these concentrations the CSF1R inhibitors did not affect the survival of the infected macrophages and reduced the intracellular bacterial replication 1 – 5 days pi. The CSF1R-specific inhibitors were more potent as compared to a less specific tyrosine kinase inhibitor Imatinib (**Fig.5D, Suppl.Fig.11C, F and I**). Previously, Imatinib has been shown to improve Mtb control in vitro and in vivo(*55*). These data suggest that within TB lesions, CSF1 can mediate a crosstalk between damaged/dysregulated epithelium and macrophages preventing macrophage maturation into efficient anti-bacterial effector cells.

V. Lung-specific TB progression

Our data suggest that lung epithelial cells may play an active, previously unrecognized, role in creating a microenvironment permissive for TB progression. In addition, the lesion progression was associated with increased hypoxia that argued against lung oxygenation as a major factor of the lung TB predilection. To determine whether oxygenation and ventilation explain the preferential lung colonization by Mtb after hematogenous spread, we implanted fragments of mouse lung tissues subcutaneously into syngeneic B6.Sst1S recipients. Spleen fragments were also implanted next to the lung, as a control (**Fig.5E** and **Suppl.Fig.12A**). After

two months, we confirmed the implant viability in a control group, and hock Mtb infected six mice carrying the implants. Using fmIHC, we confirmed that lung implants contained cells expressing lung epithelial markers: transcription factor Nkx2-1 (Ttf1), caveolin-1 (Cav1), uteroglobin, and beta-tubulin. In the lungs, Cav1 is expressed by type I alveolar epithelium and endothelium. Both cell types were present in the lung implants. Sporadic Ttf1+ (Cav1-) cells were interspersed within the interstitium, and residual bronchioles were evident by expression of non-ciliated (uteroglobin) and ciliated epithelium (beta-tubulin) (**Suppl.Fig.12B**).

At sacrifice, two mice developed advanced necrosuppurative TB lesions in both native and implanted lungs. Some lesions in lung implants were represented by organized granulomas with a necrotic core containing clusters of replicating bacteria (**Fig.5F**) surrounded by prominent fibrotic layer (**Suppl.Fig.12C**). Furthermore, only the native lungs and corresponding lung implants with advanced TB lesions contained Arg1+ macrophages, which were absent from the adjacent spleen implants (**Suppl.Fig.12D**). Only the lung implants developed advanced lesions resembling necrosuppurative pneumonia with unrestricted Mtb growth (**Suppl.Fig.12E**). Notably, only a few bacteria were found in adjacent spleen implants without granulomatous inflammation. In addition, acid fast bacilli were found in popliteal lymph nodes and spleens of these animals, but necrotizing lesions were observed exclusively in the lungs (native and implanted).

Discussion

Our results clearly demonstrate that pulmonary TB does not require direct deposition of Mtb in the lungs via aerosols and develops after hematogenous spread even in the presence of systemic immunity. Comparing the trajectories of the secondary pulmonary lesions in the resistant and susceptible mice, we describe how the bacteria gradually modify the microenvironment carving out a niche for its subsequent immune escape and replication in the

susceptible hosts. This model allows mechanistic dissection of the incipient lesions progression(*19*) that precede the formation of the more familiar advanced lesions obtained from human TB patients by surgery or at autopsies.

The paucity and heterogeneity of lung lesions in our model demonstrate that seeding the lung after hock infection and hematogenous spread are asynchronous and rare events, perhaps, not exceeding the seeding frequency in other organs. However, the structure and the dynamics of the pulmonary lesions are drastically different. Although individual lung samples for these studies were obtained at animal sacrifice and do not represent a true longitudinal timecourse experiment, the lesion classification according to pathomorphological characteristics and bacterial loads suggested stepwise progression and allowed us to make some stage-specific mechanistic inferences.

First, in contrast to primary TB after aerosol infection, the delay of local adaptive immunity does not account for the lung-specific TB progression after hematogenous dissemination. On the contrary, the incipient lung lesions that developed after several weeks post primary hock infection, were the sites of active immune responses represented by tertiary lymphoid tissue containing active B cell follicles with plasma cells, numerous T cells and activated macrophages expressing iNOS despite a very low bacterial burden. These responses and low bacterial loads were maintained in the resistant mouse lungs for at least 20 weeks p.i., protecting the host from TB progression, albeit they were insufficient to eradicate the bacteria. These stable lesions may represent an example of the “arrested” microscopic lesions that control the infection without eradication, as postulated in classical TB studies(*2, 3, 10*).

The NO production by activated macrophages is necessary for this initial control(*36*). However, it was insufficient to prevent the TB progression in the lungs of the *sst1* susceptible mice whose lesions contained abundant iNOS+ macrophages. Although the incipient lesions were similar in the wild type and *sst1*-susceptible congenic mice, gradually myeloid cells became the dominant population in the latter, perhaps via recruitment of circulating blood

monocytes and/or replication of resident macrophage populations(*56*) leading to disorganized tertiary lymphoid tissue, granulomatous pneumonia occupying airspaces and effacement of normal pulmonary parenchyma. Of note, the bacterial loads remained low. Therefore, we surmise that this stage is mostly driven by inflammatory mediators and, possibly, secreted bacterial products, but not an active bacterial replication.

At the advanced and terminal stages, we observed coalescing necrotizing pneumonia with airspaces and airways filled with innumerable neutrophils, abundant necrotic cellular debris, and profound replication of Mtb. It's feasible that larger animals could survive through this period because the pneumonic areas occupy a smaller proportion of their lungs and the spread of the coalescing necrotic lesions can be limited by the formation of a wall containing immune cells and fibrotic tissue. Eventually, after clearing the debris via airways, these pneumonic lesions would evolve into cavities, as described in human patients(*16, 17*).

The hyperinflammatory lesion progression in the *sst1* susceptible background is consistent with intrinsic dysregulation of macrophage activation described previously(*41, 57*). In vitro studies demonstrated an aberrant response of the *sst1*-susceptible macrophages to TNF, a cytokine essential for local TB resistance and granuloma maintenance (reviewed in(*58*)). This complex phenotype was characterized by unresolving oxidative and proteotoxic stress and a positive feedback regulation of the stress- and IFN-I-mediated pathways. Recently, the *sst1*-encoded SP140 protein was shown to play a major role in *sst1*-susceptibility in vivo(*59*). In human GWAS studies, the SP140 polymorphisms were associated with non-infectious inflammatory diseases - multiple sclerosis and Crohn's disease (reviewed in(*60*)). Mechanistically, it was linked to re-activation of heterochromatin and the upregulation of developmentally silenced genes, including homeobox genes, and higher overall transcriptional activity including inflammatory genes(*61*). Taken together these data demonstrate that the *sst1* locus controls the inflammatory response, but not the effectors of antimycobacterial immunity. In this context, Mtb serve as a trigger, but the subsequent phenotype amplification is driven by

myeloid cells in a cell autonomous manner via secretion of inflammatory mediators, such as IFNβ and the IFN-I-mediated chemokines, and myeloid cell recruitment. This cell-autonomous macrophage mechanism explains how dysregulated macrophage activation may compromise local immune response, despite pre-existing systemic immunity in the susceptible hosts.

To explain how Mtb induces protective systemic immunity throughout the host except in the lungs, we postulate a “two-hit” hypothesis in which (1) an aberrant macrophage response to activating stimuli and (2) the dysregulated lung repair cooperate to gradually carve a niche for Mtb replication and spread. Contrary to a common perception of TB lesions as granulomas primarily composed of immune and inflammatory cells, our data demonstrate that distal lung epithelial are intimately associated with the inflammatory cells and endure within the escalating inflammatory and hypoxic environment of the advancing TB lesions. Moreover, we found that a substantial proportion of epithelial cells clustered within advanced granulomatous lesions were phenotypically similar to Ttf1+ lung epithelial precursors and did not co-express the markers of differentiated AT2 (pro-SpC) cells, but some of these cells express pro-inflammatory mediators, such as IFNβ. In addition, we found that TB lesions contained clusters of metaplastic cytokeratin 6+ cells. These data suggest that lung parenchymal cells undergo profound changes in response to inflammatory injury and hypoxia, and in response to this non-physiological environment might produce the disease promoting factors, and further fuel the aberrant macrophage activation via short range soluble mediators and/or direct cell contacts.

Previously, lung epithelial damage and repair in non-infectious models was shown to induce the accumulation of alternatively activated macrophages that supported the epithelia regeneration(*62, 63*). We propose that the aberrant epithelial repair within TB lesions, also turns on a lung tissue-specific repair program, including the recruitment, or local differentiation, of the Arg1+ reparative macrophages. Remarkably, these alternatively activated macrophages colocalized with iNOS+ macrophages and often cloak them, similar to previously described

cloaking of tissue microlesions by resident macrophages to prevent neutrophil-driven inflammatory damage(*64*). Perhaps, these intimate interactions of the M1- and M2-like macrophages within the advanced lesions may represent a tipping point after which local host defenses crumble and the lesion progression takes a precipitous course towards the advanced non-controlling lesions.

A recently developed subcutaneous lung implant model(*65*) allowed us to compare TB progression in the lung and spleen fragments implanted side-by-side under the skin. We clearly demonstrated the formation of multibacillary TB lesions in the lung, but not in spleen implants, albeit the bacteria were found in both implants. Two lung implants contained necrotic lesions affiliated with pronounced bacterial replication. These lesions also contained Arg1+ macrophages that were absent from adjacent spleen implants, thus supporting a critical role of lung microenvironment in their recruitment and/or differentiation. Taken together, these findings point to a critical role of lung parenchymal cells in creating the Mtb permissive immune environment(*66*), and argue against high oxygenation affiliated with ventilation as a driver of pulmonary TB progression.

Hypothetically, epithelial damage, de-differentiation and metaplasia of lung epithelium described in this study may be linked to the subsequent development of squamous cell carcinomas in our model(*67*) and in human TB patients, as well as lung adenocarcinomas associated with fibrotic scars after cured pulmonary TB (scar carcinomas)(*68, 69*). Therefore, mechanisms that enable precancerous epithelial cells to promote immunosuppressive tumor associated macrophages, such as CSF1 production(*70*), may also contribute to the development of the immunosuppressive microenvironment in the “metastatic” pulmonary TB lesions and, therefore, represent novel targets for host-directed therapies.

The roles of animal models in untangling mechanisms of complex human diseases, such as TB, depend on their ability to recapitulate various clinical forms of the human disease, although no single animal model is sufficient to reproduce the complete TB spectrum.

Previously, the *sst1* susceptible mice have been instrumental in dissecting mechanisms of primary TB progression towards the formation of human-like necrotic granulomas after aerosol infection(*40, 41, 71, 72*). As shown in this study, this mutant mouse also recapitulates key morphological characteristics of post-primary TB in humans(*16*). We suggest that it is not by mere co-incidence that the *sst1* susceptible mice recapitulate the most common pathomorphological characteristics of pulmonary TB in immunocompetent humans. We propose that the *sst1* mutation reveals a common mechanism of pulmonary TB progression, where the aberrantly activated macrophages damaged by oxidative stress and hyperactivity of the type I interferon pathway drive the gradual TB progression in the lungs of immunocompetent hosts. Similar macrophage susceptibility phenotypes may be induced by environmental factors, such as smoking, air pollution, chronic viral infections, and aging. This unifying mechanism of pulmonary TB progression may explain the stealthy transformation of the initially resistant immunocompetent individuals into susceptible Mtb spreaders. Therefore, the *sst1*-susceptible mice may serve as a convenient genetically defined tool for further dissecting the multi-directional interactions between immune and structural cells in the infected lungs, and as a versatile model for testing therapeutic interventions targeting these mechanisms.

Limitations and future directions.

Having started to provide novel insights into fundamental questions of TB pathogenesis, our studies also pose key mechanistic questions. In particular, specific mechanisms by which profound changes in the epithelial cell compartment within TB lesions modify local immunity remain largely hypothetical. Are they mediated purely by secreted growth factors, such as CSF1, and cytokines, or require direct cell contact? What other resident lung cell populations are critically involved in generating the permissive microenvironment? Likely, fibrotic

mesenchymal cells induced by the aberrant epithelial repair pathways(*73*) could be a source of growth factors or potent immunosuppressive cytokines, such as IFN-I, IL-10, TGFβ and others.

The roles of lung resident macrophage populations, alveolar and interstitial, also remain to be established. We found that iNOS+ and Arg1+ macrophage populations are largely non-overlapping. What is the origin of the Arg1+ macrophages - lung resident or the recruited? What specific factors promote their appearance and propagation within pulmonary TB lesions? What are the roles of various lymphocyte populations in the crosstalk of the immune cells and structural lung cells? We believe that the described mouse model will enable further exploration of these mechanistic questions and facilitate therapeutic targeting of the unique lung vulnerability to TB.

Methods:

Reagents

Colony Stimulating Factor 1 Receptor 1 (CSF1R) inhibitors PLX3397 (Cat# S7818) and Imatinib (Cat#S2475) were purchased from Selleckchem and BLZ945 (Cat# HY-12718) was purchased from MedChemExpress. FBS for cell culture medium obtained from HyClone. Middlebrook 7H9 and 7H10 mycobacterial growth media were purchased from BD Biosciences and prepared according to manufacturers instructions. The 50 μg/mL hygromycin was used for the reporter strains (*M. tuberculosis* Erdman(SSB-GFP, smyc′::mCherry).

Animals

C57BL/6J and C3HeB/FeJ inbred mice were obtained from the Jackson Laboratory (Bar Harbor, Maine, USA). The B6J.C3-*Sst1*$^{C3HeB/Fej}$ Krmn congenic mice (B6.Sst1S) were created by transferring the sst1 susceptible allele from the C3HeB/FeJ mouse strain onto the B6

(C57BL/6J) genetic background via twelve backcrosses. These mice are referred to as B6.Sst1S in the text.

The B6.Sst1S,*ifnb*-YFP mice were produced by breeding B6.Sst1S mice with a reporter mouse containing a Yellow Fluorescent Protein (YFP) reporter gene inserted after the *Ifnb1* gene promoter(*74*). The YFP serves as a substitute for Interferon beta (IFNβ) gene expression. All experiments were conducted in accordance with relevant guidelines and regulations, with full knowledge and approval of the Standing Committee on Animals at Boston University.

BMDMs culture and Treatment

Isolation of mouse bone marrow and culture of BMDMs were carried out as previously described(*75*). BMDM were seeded in tissue culture plates. Cells were treated with CSF1R inhibitors (1 and 3 nM PLX3397, 3 and 10 nM BLZ945, imatinib 30, 100 and 300 nM) and incubated for 16-18 hours at 37°C with 5% CO_2 before Mtb infection. The media were replaced every 48 hours with fresh media and the cells were either incubated with inhibitors (Re-stimulation) or without inhibitors for additional time points at 37°C with 5% CO2.

Infection of BMDM with *M. tuberculosis*

To conduct infection experiments, M. tuberculosis H37Rv (Mtb) was grown in 7H9 liquid media for three days and then collected. The bacteria were diluted in media containing 10% L929 cell culture medium (LCCM) without antibiotics to achieve the appropriate MOI. The 100 µL of Mtb-containing media at the appropriate MOI was added to the BMDMs grown in a 96-well plate format pretreated with inhibitors. The plates were then centrifuged at 500xg for 5 minutes and then incubated for 1 hour at 37°C. To kill any extracellular bacteria, cells were treated with Amikacin at 200 µg/µL for 45 minutes. Afterward, cells were washed and cultured with inhibitors, as applicable, in DMEM/F12 containing 10% FBS medium without antibiotics at 37°C in 5% CO_2 for the duration of each experiment. Media change and replacement of inhibitors performed

every 48 hours. MOIs were confirmed by counting colonies on 7H10 agar plates. All steps involving live Mtb were performed in Biosafety Level 3 containment, in compliance with regulations from the Environmental Health and Safety at the National Emerging Infectious Disease Laboratories, the Boston Public Health Commission, and the Center for Disease Control.

Cytotoxicity and Mycobacterial growth assays

The cytotoxicity, cell loss and Mtb growth assays were performed as described in(*75*). Briefly, BMDMs were treated with inhibitors or infected with Mtb as described above for desired time points. At harvest samples were treated with Live-or-Dye™ Fixable Viability Stain (Biotium) at a 1:1000 dilution in 1X PBS/1% FBS for 30 minutes. Following staining, the samples were delicately washed to avoid any loss of dead cells from the plate, and then treated with 4% paraformaldehyde (PFA) for 30 minutes. The fixative was rinsed off, and the samples were replaced with 1X PBS. Subsequently, the sample plates were decontaminated and safely removed from containment. Using Operetta CLS HCA System (PerkinElmer), both infected and uninfected cells were counted. The intracellular bacterial load was measured via quantitative PCR (qPCR) utilizing a specific set of Mtb and *M.bovis*-BCG primer/probes with BCG spikes added as an internal control.

Generation of mice with lung and spleen implant

Lung and spleen tissue were isolated from young syngeneic (histocompatible) donor mice humanely euthanized by CO_2 asphyxiation and trimmed to approximately 5-10 mm pieces (grafts) using sterile scissors and placed into sterile tissue culture medium containing antibiotics. Mice (6 weeks of age or older) were anesthetized with isoflurane and placed in sternal recumbency. The surgical site was prepped by shaving and cleaning the area with 2% chlorhexidine and 70% ethanol in triplicate. A midline incision ~1-2 cm was made through the

skin between the scapulae of the mouse. Subcutaneous pockets were created by blunt dissection on both sides of the midline incision. Lung and spleen grafts were removed from antibiotic culture medium and dipped in Corning (Corning, NY, USA) Matrigel Basement Membrane Matrix (product number 354234). Matrigel-coated lung grafts were inserted into one subcutaneous pocket. Spleen was inserted into a contralateral side. Absorbable suture and skin glue were used to secure the incision. All mice received analgesic treatment at the time of surgery with extended-release buprenorphine (Ethiqa XR, Fidelis Pharmaceuticals LLC, North Brunswick Township, NJ) administered subcutaneously. Following recovery from anesthesia, mice were returned to colony housing with their original cage-mates, where they were monitored for signs of pain and distress post-operatively.

Infection of mice and collection of organs

The mice were anesthetized using ketamine-xylazine solution administered by intraperitoneal route. Each mouse was injected subcutaneously in the hock, the lateral tarsal region (by placing animal in the restrainer) just above the ankle with 50 µl of the 1X PBS containing 10^6 CFU of Mtb H37Rv or Mtb Erdman(SSB-GFP, smyc′::mCherry(*44*)). At desired time points the mice were anesthetized, lung perfusion performed and organs collected.

Tissue inactivation, processing, and histopathologic interpretation

Tissue samples were submersion fixed for 48 h in 10% neutral buffered formalin, processed in a Tissue-Tek VIP-5 automated vacuum infiltration processor (Sakura Finetek , Torrance, CA, USA), followed by paraffin embedding with a HistoCore Arcadia paraffin embedding machine (Leica, Wetzlar, Germany) to generate formalin-fixed, paraffin-embedded (FFPE) blocks, which were sectioned to 5 µm, transferred to positively charged slides, deparaffinized in xylene, and dehydrated in graded ethanol. A subset of slides from each sample were stained with hematoxylin and eosin (H&E) and consensus qualitative histopathology analysis was conducted

by two board-certified veterinary pathologists (N.A.C. & M.L.) to characterize the overall heterogeneity and severity of lesions.

Quantitative image analysis (pneumonia classifier and multiplex fluorescent and chromogenic immunohistochemistry)

Digitalized whole slide images (WSI) were generated for affiliated brightfield and multiplex fluorescent immunohistochemistry (mfIHC) panels were generated using a multispectral Vectra Polaris Automated Quantitative Pathology Image System (Akoya Biosciences, Marlborough, Massachusetts, USA). Quantification and classification of the pulmonary inflammatory lesions were achieved by using the HALO image analysis software v3.5 (Indica labs, Albuquerque, New Mexico, USA) random forest V2 tissue classifier. Each test image was first annotated by pathologists to define the regions of interest for subsequent image analysis. Total examined pulmonary parenchyma with associated airways were included in the regions of interest. All non-pulmonary tissues such as heart, esophagus, tracheobronchial lymph nodes, mediastinal adipose tissues, peripheral nerves, major vessels, and extra pulmonary bronchi with cartilage were excluded from the regions of interest. All cells and tissues outside the visceral pleura of the lung lobes and processing artifacts (I.e., atelectic pulmonary parenchyma resulting from insufficient postmortem lung inflation, tissue folds and dust) were also manually removed via exclusion annotations. Two classes were defined: normal and pulmonary inflammation (consolidation). The algorithm was trained on five representative cases of B6.Sst1S infected mice. The full diversity of pulmonary inflammatory spectrum was included in training, which included granulomatous pneumonia, necrosuppurative pneumonia, perivascular and peribronchiolar mononuclear infiltrates. Representative classification images are displayed in **Suppl. Fig. 2A**. The exact same classifier algorithm was applied to all cases in this study to yield the pulmonary consolidation quantification results (**Fig. 2C**).

For quantification of both chromogenic and fluorescent IHC assays using positive pixel analysis, representative areas of granulomatous pneumonia and normal parenchyma of each animal analyzed were annotated to define the regions of interest for analysis. This approach was utilized to determine the percentage of TTF-1 immunopositive areas within the areas of granulomatous pneumonia versus normal pulmonary parenchyma for each genotype. A similar approach was utilized to quantify the positive immunoreactivity area for myeloid markers (CD11b, iNOS, Arg1, and Iba1) and HIF-1α in different stages of granulomatous pneumonia across timepoints and genotypes.

For immunophenotyping and quantification of cell density the Halo HighPlex FL v4.2.3 algorithm was utilized. mfIHC slides were scanned and subsequently multispectrally unmixed using Inform software (Akoya Biosciences) using multispectral libraries. Representative areas of granulomatous pneumonia and normal parenchyma of each animal were annotated to define the regions of interest. Animals with necrosuppurative pneumonia were excluded in this analysis due to extensive necrosis in the lesions. This approach was utilized to determine the density of TTF-1^{pos} and Pro-SPC^{neg} cells in the areas of interest, as well as T and B cell densities. A summary of the optimized immunohistochemical assays is provided in **Suppl. Table 10.**

Mycobacterial staining of lung sections

To visualize mycobacteria in Mtb infected lung specimens, the brightfield acid-fast staining or auramine O-rhodamine B methods were utilized. For the brightfield acid-fast staining of Mtb infected lung sections, the new Fuchsin method (Poly Scientific R and D Corp., cat no. K093, Bay Shore, NY, USA) was used according to the manufacturer's instructions. The auramine O-rhodamine B method was performed with slight modifications to a previously described protocol(*33*). The sections were deparaffinized and rehydrated through graded ethanol washes (100%, 95%, 70%, 50%, 25% and distilled water), after which they were stained with auramine O-rhodamine B at 37◦C for 15 minutes. Excess stain was removed by washing the sections in

70% ethanol three times for 1 min each. The sections were counterstained with Mayer's hematoxylin for 5 min and washed with water. Finally, the sections were dehydrated and mounted with a permount mounting medium.

Semi-quantification of acid-fast bacilli (AFB) load

Mtb load in the lung and other tissues (I.e., spleen, popliteal lymph node, liver, and large intestines) was first qualitatively examined and subsequently an ordinal scoring system was developed to capture the overall variability in bacterial load. The ordinal criteria for the semi quantification was defined as the following: + indicates rare, individualized acid-fast bacilli (AFB) (either less than or equal to 1 per 200X field in the most severely impacted region; or there are only one to two 200X fields containing two to three individualized AFB throughout the entire section); ++ indicates sporadic single AFB with occasional chains to small clusters (more than two 200X fields contains more than 3 AFB, but AFB are not easily visible in 200X field); +++ indicates frequent clusters AFB (easily visible at 200x and even visible at 100x); ++++ indicates innumerable AFB with large clusters easily visible at 40x. **Suppl. Fig. 2B** showed representative images of Mtb load + to ++++.

Confocal immunofluorescence microscopy of tissue sections

Fixed lung lobes were embedded in a 4% agarose solution in 1X phosphate-buffered saline (PBS), and 50 µm thick sections were obtained using a Leica VT1200S vibratome. The lung sections were permeabilized by treatment with 2% Triton X-100 for 24 hours at room temperature. After permeabilization, the lung sections were washed three times for 5 minutes each with 1X PBS and then blocked in a solution of 1X PBS containing 3% bovine serum albumin (BSA) and 0.1% Triton X-100 for 1 hour at room temperature. Subsequently, the sections were incubated with primary antibodies overnight at room temperature. After primary antibody incubation, the samples were washed three times for 5 minutes each with the blocking

buffer and then incubated with secondary antibodies at room temperature for 2 hours, with all steps performed on a nutator. Following the secondary antibody incubation, the samples were washed three times for 5 minutes each with the blocking buffer, stained with Hoechst 33342 solution (Fisher Scientific) for nuclei detection, washed three times for 5 minutes each with the blocking buffer, and finally transferred into RapiClear® 1.47 solution (Sunjin Lab, Taiwan, catalog #NC1660944) for tissue clearing at room temperature on a nutator for 24 hours. The primary antibodies used were anti-TTF-1 and anti-iNOS, both at a dilution of 1:100, while Alexa Fluor 647 goat anti-rabbit antibody (from Invitrogen) was used at a dilution of 1:200 for detection.

To stain the BMDMs, 2 X 10^5 cells from B6.Sst1.S,*ifnb*-YFP were plated on sterile glass coverslips and stimulated with TNF (10 ng/ml) for 24 hours. The cells were then fixed with 4% paraformaldehyde for 15 minutes at room temperature, permeabilized with 0.25% Triton X-100 for 30 minutes and blocked for 20 minutes with 1X PBS containing 1% BSA. Next, the cells were incubated with an anti-GFP antibody (diluted 1:500) in a solution of 1% BSA in 1X PBS overnight at 4°C, followed by incubation with Alexa Fluor 546-conjugated goat anti-rabbit secondary antibody (diluted 1:1000, from Invitrogen) for 2 hours. The cells were then counter-stained with Hoechst 33342 solution for nuclei detection and mounted with ProLong Gold Antifade Mountant. All images were acquired using a Leica SP5 confocal microscope, and image processing was performed using Imaris Viewer (from Oxford Instruments) and ImageJ software (from NIH).

Statistical Analysis

To compare multiple groups with two or more variables, we employed a two-way analysis of variance (ANOVA) with adjustments made for multiple post hoc comparisons. Various comparisons were conducted in our study, including comparisons among all groups, between the control group and all other groups, and between selected groups. When comparing multiple

groups with only one variable, we utilized a one-way ANOVA and corrected for multiple post hoc comparisons. In cases where only two groups were being compared, two-tailed paired or unpaired t-tests were employed. The Log-rank (Mantel-Cox) test was used to determine the statistical significance in mouse survival data. All statistical analyses were performed using GraphPad Prism 9 software. We considered a p-value < 0.05 as statistically significant. Statistical significance is denoted using asterisks (*, $P < 0.05$; **, $P < 0.01$; ***, $P < 0.001$; ****, $P < 0.0001$).

Resource availability

Lead contact

Further information and requests for resources and reagents should be directed to and will be fulfilled by the lead contact, Igor Kramnik (ikramnik@bu.edu).

Materials availability

All unique/stable reagents generated in this study are available from the Lead Contact with a completed Materials Transfer Agreement.

Data and code availability

This study did not generate datasets/code and any additional information will be available from the lead contact upon request.

Acknowledgments

We are grateful to Drs. Roderick Bronson and Anatoly S. Gleiberman for helpful discussions of lung regeneration and carcinogenesis.

This work was supported by National Institutes of Health grant R01HL126066 (IK).

Author contributions

Conceptualization IK, SMY, LK, WRB, NC, methodology SMY, ML, SL, IG, AET, AOC, HPG, SM, ST, CET, validation and formal analysis SMY, ML, SL, AET, LK, NC, investigation SMY, SL, IG, LK, NC, resources ST, LK, NC, IK, writing – original draft SMY, NC, LK, IK, writing – review & editing IK, LK, NC, ST, WRB, supervision IK, funding acquisition IK, NC and LK

Declaration of interests

The authors declare no competing interests.

Inclusion and Diversity

We support inclusive, diverse, and equitable conduct of research.

References:

1. WHO, Global Health TB Report. *https://www.who.int/tb/publications/global_report/en/*, (2022).
2. A. R. Rich, *The pathogenesis of tuberculosis* (Thomas, Springfield, Ill.,, ed. 2d, 1951), pp. xxvii, 1028 p.
3. A. M. Dannenberg, Jr., Immunopathogenesis of pulmonary tuberculosis. *Hosp Pract (Off Ed)* **28**, 51-58 (1993).
4. S. B. Cohen, B. H. Gern, K. B. Urdahl, The Tuberculous Granuloma and Preexisting Immunity. *Annual Review of Immunology* **40**, 589-614 (2022).
5. M. Pai, M. A. Behr, D. Dowdy, K. Dheda, M. Divangahi, C. C. Boehme, A. Ginsberg, S. Swaminathan, M. Spigelman, H. Getahun, D. Menzies, M. Raviglione, Tuberculosis. *Nat Rev Dis Primers* **2**, 16076 (2016).
6. M. Orgeur, R. Brosch, Evolution of virulence in the Mycobacterium tuberculosis complex. *Curr. Opin. Microbiol.* **41**, 68-75 (2018).
7. S. Verver, R. M. Warren, N. Beyers, M. Richardson, G. D. v. d. Spuy, M. W. Borgdorff, D. A. Enarson, M. A. Behr, P. D. v. Helden, Rate of reinfection tuberculosis after successful treatment is higher than rate of new tuberculosis. *Am J Respir Crit Care Med* **171**, 1430 - 1435 (2005).
8. M. A. Behr, E. Kaufmann, J. Duffin, P. H. Edelstein, L. Ramakrishnan, Latent Tuberculosis: Two Centuries of Confusion. *American Journal of Respiratory and Critical Care Medicine* **204**, 142-148 (2021).
9. V. Balasubramanian, E. H. Wiegeshaus, B. T. Taylor, D. W. Smith, Pathogenesis of tuberculosis: pathway to apical localization. *Tuber. Lung Dis.* **75**, 168-178 (1994).
10. D. N. McMurray, F. M. Collins, A. M. Dannenberg, Jr., D. W. Smith, Pathogenesis of experimental tuberculosis in animal models. *Curr Top Microbiol Immunol* **215**, 157-179 (1996).
11. R. J. North, Y.-J. Jung, Immunity to Tuberculosis. *Immunology* **22**, 599-623 (2004).
12. M. G. Moule, J. D. Cirillo, Mycobacterium tuberculosis Dissemination Plays a Critical Role in Pathogenesis. *Frontiers in Cellular and Infection Microbiology* **10**, 492 (2020).
13. R. Verma, B. M. C. Swift, W. Handley-Hartill, J. K. Lee, G. Woltmann, C. E. D. Rees, P. Haldar, A Novel, High-sensitivity, Bacteriophage-based Assay Identifies Low-level Mycobacterium tuberculosis Bacteremia in Immunocompetent Patients With Active and Incipient Tuberculosis. *Clin. Infect. Dis.* **70**, 933-936 (2019).
14. R. L. Hunter, The Pathogenesis of Tuberculosis: The Early Infiltrate of Post-primary (Adult Pulmonary) Tuberculosis: A Distinct Disease Entity. *Frontiers in Immunology* **9**, 2108 (2018).
15. D. N. McMurray, Hematogenous reseeding of the lung in low-dose, aerosol-infected guinea pigs: unique features of the host–pathogen interface in secondary tubercles. *Tuberculosis* **83**, 131-134 (2003).
16. R. L. Hunter, Pathology of post primary tuberculosis of the lung: An illustrated critical review. *Tuberculosis* **91**, 497 - 509 (2011).
17. G. Wells, J. N. Glasgow, K. Nargan, K. Lumamba, R. Madansein, K. Maharaj, R. L. Hunter, T. Naidoo, L. Coetzer, S. l. Roux, A. d. Plessis, A. J. C. Steyn, Micro–Computed Tomography Analysis of the Human Tuberculous Lung Reveals Remarkable Heterogeneity in Three-dimensional Granuloma Morphology. *American Journal of Respiratory and Critical Care Medicine* **204**, 583-595 (2021).

18. R. L. Hunter, The Pathogenesis of Tuberculosis–The Koch Phenomenon Reinstated. *Pathogens* **9**, 813 (2020).
19. P. K. Drain, K. L. Bajema, D. Dowdy, K. Dheda, K. Naidoo, S. G. Schumacher, S. Ma, E. Meermeier, D. M. Lewinsohn, D. R. Sherman, Incipient and Subclinical Tuberculosis: a Clinical Review of Early Stages and Progression of Infection. *Clin Microbiol Rev* **31**, (2018).
20. T. S. Ryckman, D. W. Dowdy, E. A. Kendall, Infectious and clinical tuberculosis trajectories: Bayesian modeling with case finding implications. *Proceedings of the National Academy of Sciences* **119**, e2211045119 (2022).
21. D. L. Barber, The Helper T Cell's Dilemma in Tuberculosis. *Cell Host Microbe* **21**, 655-656 (2017).
22. K. D. Kauffman, M. A. Sallin, S. Sakai, O. Kamenyeva, J. Kabat, D. Weiner, M. Sutphin, D. Schimel, L. Via, C. E. Barry, 3rd, T. Wilder-Kofie, I. Moore, R. Moore, D. L. Barber, Defective positioning in granulomas but not lung-homing limits CD4 T-cell interactions with Mycobacterium tuberculosis-infected macrophages in rhesus macaques. *Mucosal Immunol* **11**, 462-473 (2018).
23. S. M. Behar, S. M. Carpenter, M. G. Booty, D. L. Barber, P. Jayaraman, Orchestration of pulmonary T cell immunity during Mycobacterium tuberculosis infection: immunity interruptus. *Seminars in Immunology* **26**, 559 - 577 (2014).
24. J. D. Ernst, Mechanisms of M. tuberculosis Immune Evasion as Challenges to TB Vaccine Design. *Cell host & microbe* **24**, 34 - 42 (2018).
25. J. D. Ernst, Mechanisms of M. tuberculosis Immune Evasion as Challenges to TB Vaccine Design. *Cell host & microbe* **24**, 34-42 (2018).
26. P. Andersen, T. J. Scriba, Moving tuberculosis vaccines from theory to practice. *Nature Publishing Group* **19**, 550 - 562 (2019).
27. I. Comas, J. Chakravartti, P. M. Small, J. Galagan, S. Niemann, K. Kremer, J. D. Ernst, S. Gagneux, Human T cell epitopes of Mycobacterium tuberculosis are evolutionarily hyperconserved. *Nature genetics* **42**, 498 - 503 (2010).
28. P. Ogongo, J. D. Ernst, Finding antigens for TB vaccines: the good, the bad and the useless. *Nature Medicine* **29**, 35-36 (2023).
29. H. E. Volkman, T. C. Pozos, J. Zheng, J. M. Davis, J. F. Rawls, L. Ramakrishnan, Tuberculous granuloma induction via interaction of a bacterial secreted protein with host epithelium. *Science* **327**, 466-469.
30. A. M. d. Waal, P. S. Hiemstra, T. H. M. Ottenhoff, S. A. Joosten, A. M. v. d. Does, Lung epithelial cells interact with immune cells and bacteria to shape the microenvironment in tuberculosis. *Thorax* **77**, 408-416 (2022).
31. H. P. Gideon, T. K. Hughes, C. N. Tzouanas, M. H. Wadsworth, A. A. Tu, T. M. Gierahn, J. M. Peters, F. F. Hopkins, J.-R. Wei, C. Kummerlowe, N. L. Grant, K. Nargan, J. Y. Phuah, H. J. Borish, P. Maiello, A. G. White, C. G. Winchell, S. K. Nyquist, S. K. C. Ganchua, A. Myers, K. V. Patel, C. L. Ameel, C. T. Cochran, S. Ibrahim, J. A. Tomko, L. J. Frye, J. M. Rosenberg, A. Shih, M. Chao, E. Klein, C. A. Scanga, J. Ordovas-Montanes, B. Berger, J. T. Mattila, R. Madansein, J. C. Love, P. L. Lin, A. Leslie, S. M. Behar, B. Bryson, J. L. Flynn, S. M. Fortune, A. K. Shalek, Multimodal profiling of lung granulomas in macaques reveals cellular correlates of tuberculosis control. *Immunity*, (2022).

32. L. Desvignes, J. D. Ernst, Interferon-gamma-responsive nonhematopoietic cells regulate the immune response to Mycobacterium tuberculosis. *Immunity* **31**, 974-985 (2009).
33. B. S. Yan, A. V. Pichugin, O. Jobe, L. Helming, E. B. Eruslanov, J. A. Gutierrez-Pabello, M. Rojas, Y. V. Shebzukhov, L. Kobzik, I. Kramnik, Progression of pulmonary tuberculosis and efficiency of bacillus Calmette-Guerin vaccination are genetically controlled via a common sst1-mediated mechanism of innate immunity. *J Immunol* **179**, 6919-6932 (2007).
34. S. T. Reece, C. Loddenkemper, D. J. Askew, U. Zedler, S. Schommer-Leitner, M. Stein, F. A. Mir, A. Dorhoi, H.-J. Mollenkopf, G. A. Silverman, S. H. E. Kaufmann, Serine protease activity contributes to control of Mycobacterium tuberculosis in hypoxic lung granulomas in mice. *The Journal of clinical investigation* **120**, 3365 - 3376 (2010).
35. J. Nemeth, G. S. Olson, A. C. Rothchild, A. N. Jahn, D. Mai, F. J. Duffy, J. L. Delahaye, S. Srivatsan, C. R. Plumlee, K. B. Urdahl, E. S. Gold, A. Aderem, A. H. Diercks, Contained Mycobacterium tuberculosis infection induces concomitant and heterologous protection. *PLoS pathogens* **16**, e1008655 (2020).
36. M. Gengenbacher, M. A. Duque-Correa, P. Kaiser, S. Schuerer, D. Lazar, U. Zedler, S. T. Reece, A. Nayyar, S. T. Cole, V. Makarov, C. E. B. Iii, V. Dartois, S. H. E. Kaufmann, NOS2-deficient mice with hypoxic necrotizing lung lesions predict outcomes of tuberculosis chemotherapy in humans. *Sci Rep-uk* **7**, 514 - 510 (2017).
37. A. Kupz, U. Zedler, M. Stäber, S. H. E. Kaufmann, A Mouse Model of Latent Tuberculosis Infection to Study Intervention Strategies to Prevent Reactivation. *PloS one* **11**, e0158849 (2016).
38. I. Kramnik, W. F. Dietrich, P. Demant, B. R. Bloom, Genetic control of resistance to experimental infection with virulent Mycobacterium tuberculosis. *Proc Natl Acad Sci U S A* **97**, 8560-8565 (2000).
39. A. V. Pichugin, B.-S. Yan, A. Sloutsky, L. Kobzik, I. Kramnik, Dominant role of the sst1 locus in pathogenesis of necrotizing lung granulomas during chronic tuberculosis infection and reactivation in genetically resistant hosts. *The American journal of pathology* **174**, 2190-2201 (2009).
40. H. Pan, B.-S. Yan, M. Rojas, Y. V. Shebzukhov, H. Zhou, L. Kobzik, D. E. Higgins, M. J. Daly, B. R. Bloom, I. Kramnik, Ipr1 gene mediates innate immunity to tuberculosis. *Nature* **434**, 767-772 (2005).
41. B. Bhattacharya, S. Xiao, S. Chatterjee, M. Urbanowski, A. Ordonez, E. A. Ihms, G. Agrahari, S. Lun, R. Berland, A. Pichugin, Y. Gao, J. Connor, A. R. Ivanov, B. S. Yan, L. Kobzik, B. B. Koo, S. Jain, W. Bishai, I. Kramnik, The integrated stress response mediates necrosis in murine Mycobacterium tuberculosis granulomas. *J Clin Invest* **131**, (2021).
42. T. Kamala, Hock immunization: a humane alternative to mouse footpad injections. *Journal of immunological methods* **328**, 204 - 214 (2007).
43. A. S. Apt, I. B. Kramnik, A. M. Moroz, Regulation of T-cell proliferative responses by cells from solid lung tissue of M. tuberculosis-infected mice. *Immunology* **73**, 173-179 (1991).
44. R. C. Lavin, S. Tan, Spatial relationships of intra-lesion heterogeneity in Mycobacterium tuberculosis microenvironment, replication status, and drug efficacy. *PLOS Pathogens* **18**, e1010459 (2022).

45. M. V. Kuleshov, M. R. Jones, A. D. Rouillard, N. F. Fernandez, Q. Duan, Z. Wang, S. Koplev, S. L. Jenkins, K. M. Jagodnik, A. Lachmann, M. G. McDermott, C. D. Monteiro, G. W. Gundersen, A. Ma'ayan, Enrichr: a comprehensive gene set enrichment analysis web server 2016 update. *Nucleic Acids Research* **44**, W90-W97 (2016).
46. A. E. Vaughan, A. N. Brumwell, Y. Xi, J. E. Gotts, D. G. Brownfield, B. Treutlein, K. Tan, V. Tan, F. C. Liu, M. R. Looney, M. a. Matthay, J. R. Rock, H. A. Chapman, Lineage-negative progenitors mobilize to regenerate lung epithelium after major injury. *Nature* **517**, 621 - 625 (2015).
47. J. J. Kathiriya, A. N. Brumwell, J. R. Jackson, X. Tang, H. A. Chapman, Distinct Airway Epithelial Stem Cells Hide among Club Cells but Mobilize to Promote Alveolar Regeneration. *Cell Stem Cell* **26**, 346-358.e344 (2020).
48. L. Moreira-Teixeira, K. Mayer-Barber, A. Sher, A. O'Garra, Type I interferons in tuberculosis: Foe and occasionally friend. *The Journal of experimental medicine* **215**, 1273 - 1285 (2018).
49. X. Yang, Z. An, Z. Hu, J. Xi, C. Dai, Y. Zhu, Expression Analysis of Ligand-Receptor Pairs Identifies Cell-to-Cell Crosstalk between Macrophages and Tumor Cells in Lung Adenocarcinoma. *J Immunol Res* **2022**, 9589895 (2022).
50. S. M. Pyonteck, L. Akkari, A. J. Schuhmacher, R. L. Bowman, L. Sevenich, D. F. Quail, O. C. Olson, M. L. Quick, J. T. Huse, V. Teijeiro, M. Setty, C. S. Leslie, Y. Oei, A. Pedraza, J. Zhang, C. W. Brennan, J. C. Sutton, E. C. Holland, D. Daniel, J. A. Joyce, CSF-1R inhibition alters macrophage polarization and blocks glioma progression. *Nature medicine* **19**, 1264 - 1272 (2013).
51. F. Klemm, J. A. Joyce, Microenvironmental regulation of therapeutic response in cancer. *Trends in cell biology* **25**, 198 - 213 (2015).
52. N. Hagan, J. L. Kane, D. Grover, L. Woodworth, C. Madore, J. Saleh, J. Sancho, J. Liu, Y. Li, J. Proto, M. Zelic, A. Mahan, M. Kothe, A. A. Scholte, M. Fitzgerald, B. Gisevius, A. Haghikia, O. Butovsky, D. Ofengeim, CSF1R signaling is a regulator of pathogenesis in progressive MS. *Cell Death Dis* **11**, 904 (2020).
53. A. Olmos-Alonso, S. T. T. Schetters, S. Sri, K. Askew, R. Mancuso, M. Vargas-Caballero, C. Holscher, V. H. Perry, D. Gomez-Nicola, Pharmacological targeting of CSF1R inhibits microglial proliferation and prevents the progression of Alzheimer's-like pathology. *Brain*, awv379 (2016).
54. C. V. Jones, S. D. Ricardo, Macrophages and CSF-1. *Organogenesis* **9**, 249-260 (2013).
55. Ruth J. Napier, W. Rafi, M. Cheruvu, Kimberly R. Powell, M. A. Zaunbrecher, W. Bornmann, P. Salgame, Thomas M. Shinnick, D. Kalman, Imatinib-Sensitive Tyrosine Kinases Regulate Mycobacterial Pathogenesis and Represent Therapeutic Targets against Tuberculosis. *Cell Host & Microbe* **10**, 475-485 (2011).
56. S. J. Jenkins, D. Ruckerl, P. C. Cook, L. H. Jones, F. D. Finkelman, N. v. Rooijen, A. S. MacDonald, J. E. Allen, Local macrophage proliferation, rather than recruitment from the blood, is a signature of TH2 inflammation. *Science* **332**, 1284 - 1288 (2011).
57. E. Brownhill, S. M. Yabaji, V. Zhernovkov, O. S. Rukhlenko, K. Seidel, B. Bhattacharya, S. Chatterjee, H. A. Chen, N. Crossland, W. Bishai, B. N. Kholodenko, A. Gimelbrant, L. Kobzik, I. Kramnik, Maladaptive oxidative stress cascade drives type I interferon hyperactivity in TNF activated macrophages promoting necrosis in murine tuberculosis granulomas. *bioRxiv*, 2020.2012.2014.422743 (2020).

58. J. L. Flynn, J. Chan, Immune cell interactions in tuberculosis. *Cell* **185**, 4682-4702 (2022).
59. D. X. Ji, K. C. Witt, D. I. Kotov, S. R. Margolis, A. Louie, V. Chevee, K. J. Chen, M. M. Gaidt, H. S. Dhaliwal, A. Y. Lee, S. L. Nishimura, D. S. Zamboni, I. Kramnik, D. A. Portnoy, K. H. Darwin, R. E. Vance, Role of the transcriptional regulator SP140 in resistance to bacterial infections via repression of type I interferons. *Elife* **10**, (2021).
60. I. Fraschilla, K. L. Jeffrey, The Speckled Protein (SP) Family: Immunity's Chromatin Readers. *Trends Immunol* **41**, 572-585 (2020).
61. S. Mehta, D. A. Cronkite, M. Basavappa, T. L. Saunders, F. Adiliaghdam, H. Amatullah, S. A. Morrison, J. D. Pagan, R. M. Anthony, P. Tonnerre, G. M. Lauer, J. C. Lee, S. Digumarthi, L. Pantano, S. J. H. Sui, F. Ji, R. Sadreyev, C. Zhou, A. C. Mullen, V. Kumar, Y. Li, C. Wijmenga, R. J. Xavier, T. K. Means, K. L. Jeffrey, Maintenance of macrophage transcriptional programs and intestinal homeostasis by epigenetic reader SP140. *Sci Immunol* **2**, (2017).
62. M. C. Basil, J. Katzen, A. E. Engler, M. Guo, M. J. Herriges, J. J. Kathiriya, R. Windmueller, A. B. Ysasi, W. J. Zacharias, H. A. Chapman, D. N. Kotton, J. R. Rock, H.-W. Snoeck, G. Vunjak-Novakovic, J. A. Whitsett, E. E. Morrisey, The Cellular and Physiological Basis for Lung Repair and Regeneration: Past, Present, and Future. *Cell Stem Cell* **26**, 482-502 (2020).
63. A. E. Engler, A. B. Ysasi, R. M. F. Pihl, C. Villacorta-Martin, H. M. Heston, H. M. K. Richardson, B. R. Thapa, N. R. Moniz, A. C. Belkina, S. A. Mazzilli, J. R. Rock, Airway-Associated Macrophages in Homeostasis and Repair. *Cell Reports* **33**, 108553 (2020).
64. S. Uderhardt, A. J. Martins, J. S. Tsang, T. Lämmermann, R. N. Germain, Resident Macrophages Cloak Tissue Microlesions to Prevent Neutrophil-Driven Inflammatory Damage. *Cell* **177**, 541 - 555.e517 (2019).
65. A. Wahl, C. De, M. A. Fernandez, E. M. Lenarcic, Y. Xu, A. S. Cockrell, R. A. Cleary, C. E. Johnson, N. J. Schramm, L. M. Rank, I. G. Newsome, H. A. Vincent, W. Sanders, C. R. Aguilera-Sandoval, A. Boone, W. H. Hildebrand, P. A. Dayton, R. S. Baric, R. J. Pickles, M. Braunstein, N. J. Moorman, N. Goonetilleke, J. V. Garcia, Precision mouse models with expanded tropism for human pathogens. *Nature Biotechnology* **37**, 1163-1173 (2019).
66. T. Krausgruber, N. Fortelny, V. Fife-Gernedl, M. Senekowitsch, L. C. Schuster, A. Lercher, A. Nemc, C. Schmidl, A. F. Rendeiro, A. Bergthaler, C. Bock, Structural cells are key regulators of organ-specific immune responses. *Nature* **583**, 296-302 (2020).
67. A. Nalbandian, B. S. Yan, A. Pichugin, R. T. Bronson, I. Kramnik, Lung carcinogenesis induced by chronic tuberculosis infection: the experimental model and genetic control. *Oncogene* **28**, 1928-1938 (2009).
68. R. K. Bobba, J. S. Holly, T. Loy, M. C. Perry, Scar carcinoma of the lung: a historical perspective. *Clinical lung cancer* **12**, 148 - 154 (2011).
69. M. Irfan, Post-tuberculosis pulmonary function and noninfectious pulmonary disorders. *International journal of mycobacteriology* **5 Suppl 1**, S57 (2016).
70. M. A. Cannarile, M. Weisser, W. Jacob, A.-M. Jegg, C. H. Ries, D. Rüttinger, Colony-stimulating factor 1 receptor (CSF1R) inhibitors in cancer therapy. *Journal for ImmunoTherapy of Cancer* **5**, 705 (2017).
71. I. Kramnik, Genetic dissection of host resistance to Mycobacterium tuberculosis: the sst1 locus and the Ipr1 gene. *Curr Top Microbiol Immunol* **321**, 123-148 (2008).

72. D. X. Ji, L. H. Yamashiro, K. J. Chen, N. Mukaida, I. Kramnik, K. H. Darwin, R. E. Vance, Type I interferon-driven susceptibility to Mycobacterium tuberculosis is mediated by IL-1Ra. *Nat Microbiol* **4**, 2128-2135 (2019).
73. M. Cassandras, C. Wang, J. Kathiriya, T. Tsukui, P. Matatia, M. Matthay, P. Wolters, A. Molofsky, D. Sheppard, H. Chapman, T. Peng, Gli1+ mesenchymal stromal cells form a pathological niche to promote airway progenitor metaplasia in the fibrotic lung. *Nature Cell Biology* **22**, 1295-1306 (2020).
74. S. Scheu, P. Dresing, R. M. Locksley, Visualization of IFNβ production by plasmacytoid versus conventional dendritic cells under specific stimulation conditions in vivo. *Proceedings of the National Academy of Sciences of the United States of America* **105**, 20416-20421 (2008).
75. S. M. Yabaji, S. Chatterjee, E. Waligursky, A. Gimelbrant, I. Kramnik, Medium throughput protocol for genome-based quantification of intracellular mycobacterial loads and macrophage survival during in vitro infection. *Star Protoc* **3**, 101241 (2022).

Figure legends:

Figure 1. TB dissemination to regional popliteal lymph node and progression in the lungs of B6.Sst1S mice

A. Representative histopathology and AFB load in popliteal lymph node of B6.Sst1S mouse at 6 weeks post hock infection with 10^6 CFU of Mtb Erdman

Left panel - clusters of macrophages (microgranulomas) scattered in the peri-trabecular and medullary sinuses of popliteal lymph node (H&E stain, 100X). Middle – microgranuloma (H&E stain, 400X). Right panel - Ziehl-Neelsen acid fast stain, 400X. A few acid-fast bacilli (arrowhead) are scattered in the clusters of macrophages.

B-D. Lung lesions in B6.Sst1S mice representing stages of TB from early to necrotic lesions

Lung pathology in post-primary pulmonary tuberculosis (pppTB) post subcutaneous (SQ) hock inoculation 12 weeks post-inoculation. Top row-sub gross whole lung sections; middle row-high magnification images of black hashed boxes indicated in sub gross images; bottom row-representative image of acid-fast bacilli (AFB) load in each respective stage.

B - Stage I – interstitial granulomatous lesions are small and less frequent, with rare residual single AFB (left column).

C - Stage II - more advanced granulomatous lesions with the presence of more numerous intracellular bacteria, expansion of myeloid cells and partial disorganization of lymphoid follicles (middle column).

D - Stage III – extensive granulomatous pneumonia with the presence of cholesterol clefts, neutrophils associated with areas of micronecrosis, and cords of proliferating intracellular and extracellular AFB (right column).

Figure 2. The *sst1* locus drives pulmonary TB progression

A. Survival curves of mice infected with *M. tuberculosis*. Survival of B6 (n=12) and B6.Sst1S (n=37) following hock infection with 10^6 CFU of Mtb Erdman(SSB-GFP, smyc′::mCherry). The Log-rank (Mantel-Cox) test was applied to determine the statistical significance.

B. Percent weight gain in mice infected with M. tuberculosis. Percent weight gain of B6 (n=12) and B6.Sst1S (n=37) following hock infection with 10^6 CFU of Mtb Erdman(SSB-GFP, smyc′::mCherry). The statistical significance was performed by two-way ANOVA using Tukey's multiple comparison test.

C. Inflammation quantification, orange dots denote the B6.Sst1S mice with necrosuppurative pneumonia.

D. Mtb loads in organs of B6.Sst1S and B6 mice. Each hash on the X-axis represents individual mouse.

E. Representative histopathology and AFB load of infected C57BL/6J at 11 and 20 weeks post infection. Left two columns: H&E stain, 100X. Right two columns: Ziehl-Neelsen acid fast stain, 400X.

F. Early TB lung lesions in B6 (left column) and B6.Sst1S (right column) mice with prominent lymphoid follicles. Top raw H&E. Arrows - plasma cells and multinucleated cell.
Middle and low rows - fmIHC of early lesions, low and high magnification, respectively.

G. Representative images B6.Sst1S controlling (C) vs non-controlling (NC) lung lesions at 100X magnification.

H. 3D confocal images of thick lung sections (50 μm) from B6.Sst1S mice containing controlling vs non-controlling lesions. Mtb Erdman(SSB-GFP, *smyc'*::mCherry - red, iNOS staining - teal, and nuclei (DAPI) - gray. Scale bar- 50μm

I. Comparisons of T and B cell densities and Iba1^{+}, iNOS^{+}, Arg1^{+} and Iba1^{+}iNOS^{-}Arg^{-} area quantification in B6 controlling (n=6), B6.Sst1S controlling (n=5) and B6.Sst1S non-controlling (n=5) lesions. Data are expressed on scatter dot plots with medians. Each data point represents a single animal. The statistical significance was performed by two-way ANOVA using Tukey's multiple comparison test.

The p value <0.05 was considered statistically significant. Significant differences are indicated with asterisks (*, P < 0.05; **, P < 0.01; ***, P < 0.001; ****, P < 0.0001).

Figure 3. Progression of pulmonary TB lesions in the *sst1* susceptible B6.Sst1S and (HeBxB6.Sst1S) F1 hybrid mice.

A. Representative images of non-controlling Intermediate (NC-I) from F1 hybrid and non-controlling advanced (NC-A) from B6.Sst1S lung TB lesions: H&E (top row), acid-fast bacilli (AFB) (middle row) and CD11b immunohistochemistry (bottom row) at 14wpi. The NC-A lesions had areas of micronecrosis, neutrophilic influx, and AFB (quantitative analysis – Supplemental Fig.6E and 6F).

B. Heatmaps of GeoMx spatial transciptomic analysis comparing uninvolved (U) lung, NC-I from F1 lesions and NC-A from B6.Sst1S lung lesions. Lung lobes were selected from 2 mice with paucibacilarly NC-I lesions and 2 mice with multibacillary NC-A lesions with micronecrotic areas. The four lobes were assembled on one slide and processed in parallel. Slides were

stained with CD45-, pan-keratin-specific antibodies and DAPI. Gene expression, Red-High and Blue-Low.

C. Representative fluorescent multiplex immunohistochemistry (fmIHC) of NC-I (left) and NC-A (right) lesions. Arginase 1 (Arg1) - yellow ; inducible nitric oxide (iNOS) -teal; ionized calcium-binding adaptor molecule 1 (Iba1) - blue; CD19 - green; CD3 epsilon (CD3ε) - red. 200x total magnification.

D. Cellular composition of the uninvolved (U), NC-I) and NC-A lesions by deconvolution of GeoMxspatial transcriptomics data using CYBERsort algorithm.

E. Nuclear HIF1α staining of NC-I vs NC-A lesions. Representative immunohistochemistry images of hypoxia-inducible factor 1-alpha (HIF-1α) expression in Int and Adv TB lesions. 200x total magnification.

F. Macrophage polarization in NC-I vs NC-A lesions in B6.Sst1S: fmIHC staining iNOS (teal) and Arg1 (yellow).

G. Quantitative analysis of iNOS+Arg1-, iNOS-Arg1+ and iNOS+Arg1+ cells in F.

H. High magnification of interacting Arg1- (yellow) and iNOS (teal) – expressing macrophages. T cells – red, Iba1+iNOS-Arg1- macrophages – blue.

Figure 4. Characterization of lung epithelial cells in TB lesions

A. An example of a region of interest (ROI) selection from non-controlling pppTB lesion. Staining – pan cytokeratin (green) and CD45 (blue)

B. Expression of the lung epithelial cell markers TTF-1, Pro-SPC (AT-II) and Caveolin-1(AT-I) in uninvolved lung (left) and granulomatous lung lesion (right).

C. Cells expressing the *ifnb*-YFP reporter in the lesions of B6.Sst1S,*ifnb*-YFP mice. YFP-expressing cells were detected using anti-GFP antibodies (GFP+). GFP expression was detected primarily in iNOS expressing macrophages but also in TTF-1^{Pos}Pro-SPC^{neg} lung epithelial cells (white boxes). Scale bar- 50µm

D. mfIHC quantitative comparison of total numbers of cells with positive nuclear immunoreactivity of TTF-1 and negative cytoplasmic immunoreactivity of Pro-SPC (TTF-1^{Pos}Pro-SPC^{neg}) determined by phenotyping algorithm per 10^4 μm^2 area analyzed in the representative normal pulmonary parenchyma (unaffected, UN) versus areas of granulomatous pneumonia (Lesion). Pair data from six Mtb-infected B6.Sst1S,*ifnb*-YFP reporter mice presented with Mtb load of ++ to ++++ were included in this analysis (p=0.0018). Statistical test applied?

E. 3D confocal images of cleared thick lung sections (50 µm) of the TB lesion of B6.Sst1S,*ifnb*-YFP mice. Endogenous YFP is shown in green, TTF-1 staining - in magenta, and reporter Mtb (*smyc'* :: mCherry) in red . Left image - all the stacks in 3D, on the right – individual images of TTF-1+ cells expressing YFP (denoted by white boxes on the left panel). Scale bar-50µm

F. 3D confocal images of cleared thick lung sections (50 µm) of the TB lesion of B6.Sst1S,*ifnb*-YFP mice. Endogenous YFP is shown in green, iNOS staining - in teal, and reporter Mtb (*smyc'*

:: mCherry) in red . Left image - all the stacks in 3D, on the right – individual images of iNOS+ cells expressing YFP (denoted by white box on the left panel). Scale bar- 50µm

Figure 5. Lung epithelial cells promote the progression of TB lesions

A. An example of the lung epithelial cell (panCK+, green) selection within ROI for GeoMx spatial transcriptome analysis.

B. Pathways upregulated in epithelial cells within the NC-A as compared to NC-I lesions

C. Heatmap of genes encoding soluble mediators that are differentially expressed by panCK+ cells in NC-A vs NC-I TB lesions identified using GeoMx spatial analysis. Gene expression, Red-High and Blue-Low.

D. Effects of CSF1R inhibitors on Mtb control by B6.Sst1S BMDMs. B6.Sst1S BMDM were treated with CSF1R inhibitors, PLX3397 (1, 3 nM), BLZ945 (3, 10 nM) and imatinib (30, 100 and 300 nM) for 16 h followed by infection with Mtb Erdman at MOI=1. The Mtb loads were quantified by PCR based method and represented as Mtb load as compared to percentage in untreated at day 5 post infection. The dotted line indicates the percent Mtb load in untreated group (100%). The p value <0.05 was considered statistically significant and Dunnett's multiple comparisons test was used to determine statistical differences.

E. Adjacent lung (left) and spleen (right) implants under the mouse skin. Left image - H&E. Original magnification - 100X. Right image – fmIHC revealing lung epithelial cells (TTF-

1+) exclusively in lung implants and Iba1+ macrophages in both spleen and lung implants. Organized necrotic granuloma in the lung implant is marked by star.

F. Representative hematoxylin and eosin (H&E) and acid-fast bacilli (AFB) staining of lung and spleen implants. Lung implant with a focal caseating granuloma surrounded by collagen (left, top) with innumerable AFB (left, bottom). Spleen implants were typically histologically normal (left, top) which was affiliated with absence of detectable AFB (right, bottom). 200x total magnification.

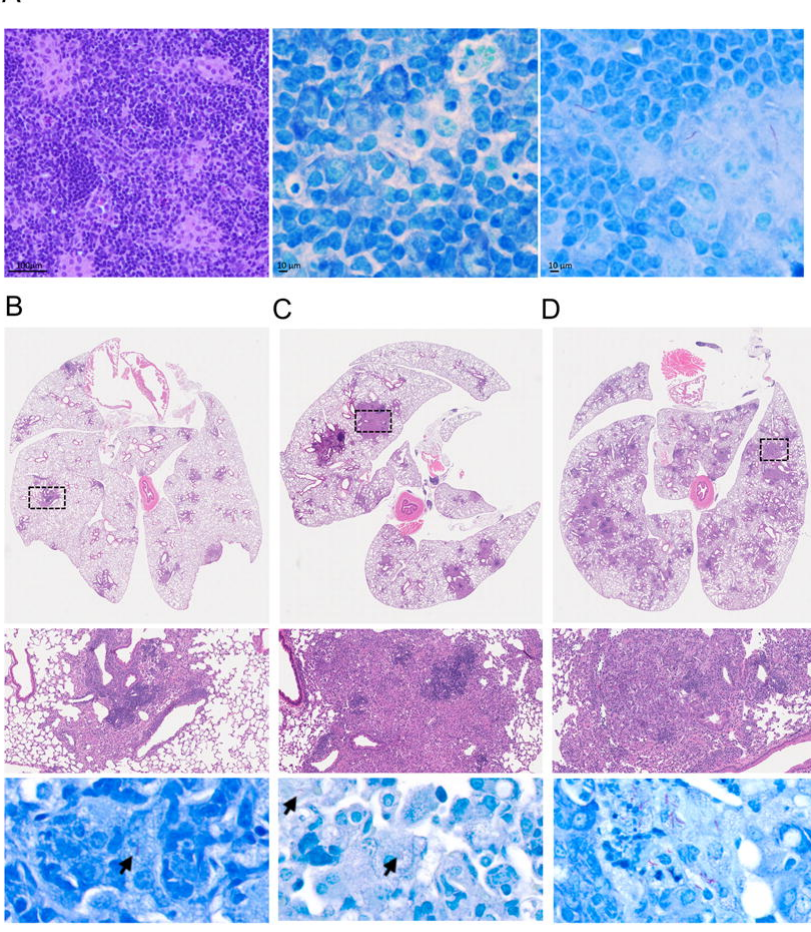

Figure 1

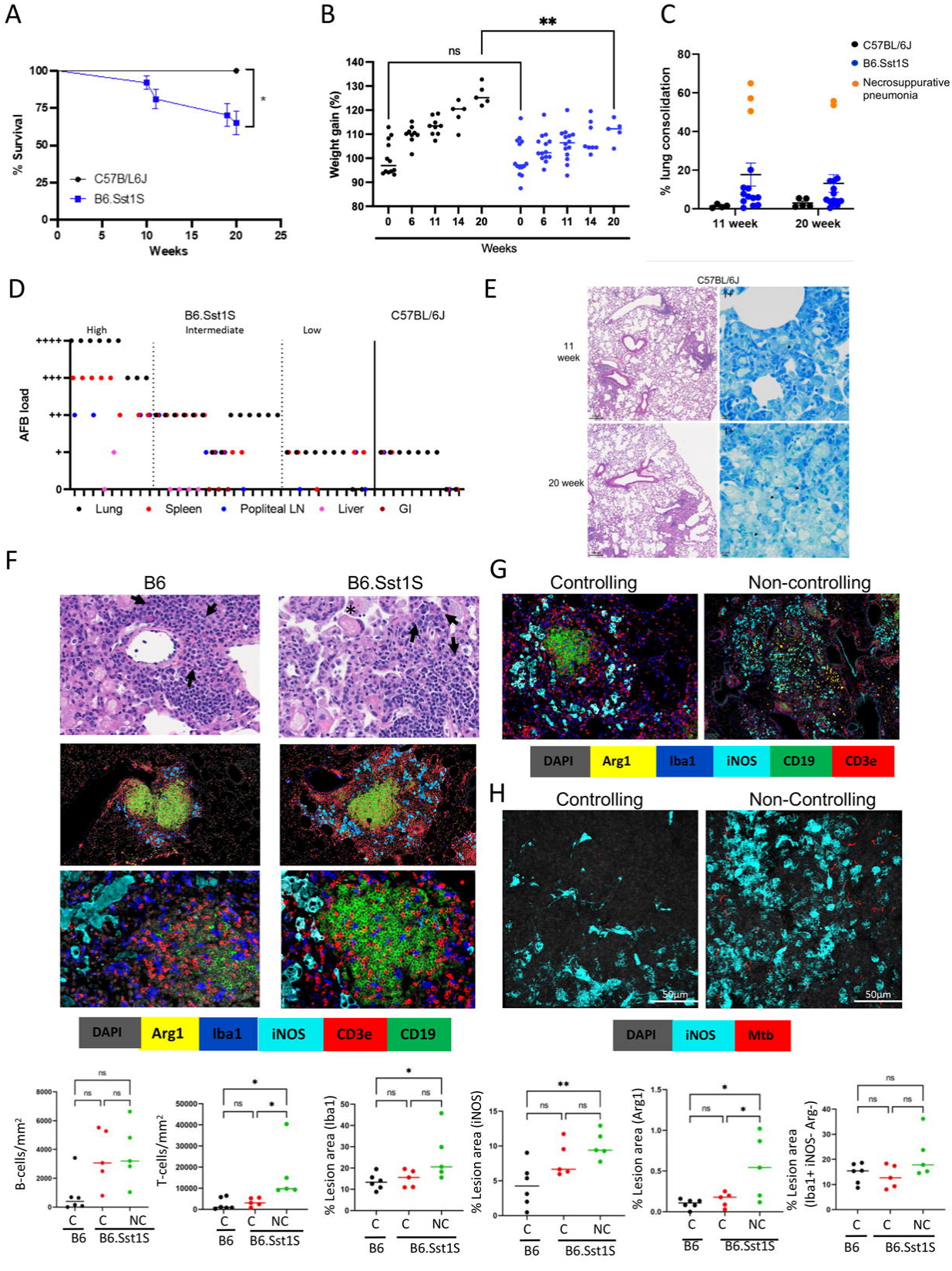
A
% Survival
Weeks
C57B/L6J
B6.Sst1S
B
Weight gain (%)
ns
**
Weeks
C
% lung consolidation
C57BL/6J
B6.Sst1S
Necrosuppurative pneumonia
11 week
20 week
D
B6.Sst1S
C57BL/6J
High
Intermediate
Low
AFB load
Lung
Spleen
Popliteal LN
Liver
GI
E
C57BL/6J
11 week
20 week
F
B6
B6.Sst1S
DAPI
Arg1
Iba1
iNOS
CD3e
CD19
G
Controlling
Non-controlling
DAPI
Arg1
Iba1
iNOS
CD19
CD3e
H
Controlling
Non-Controlling
50µm
DAPI
iNOS
Mtb
I
B-cells/mm²
T-cells/mm²
% Lesion area (Iba1)
% Lesion area (iNOS)
% Lesion area (Arg1)
% Lesion area (Iba1+ iNOS- Arg-)
C
NC
B6
B6.Sst1S

Figure 2

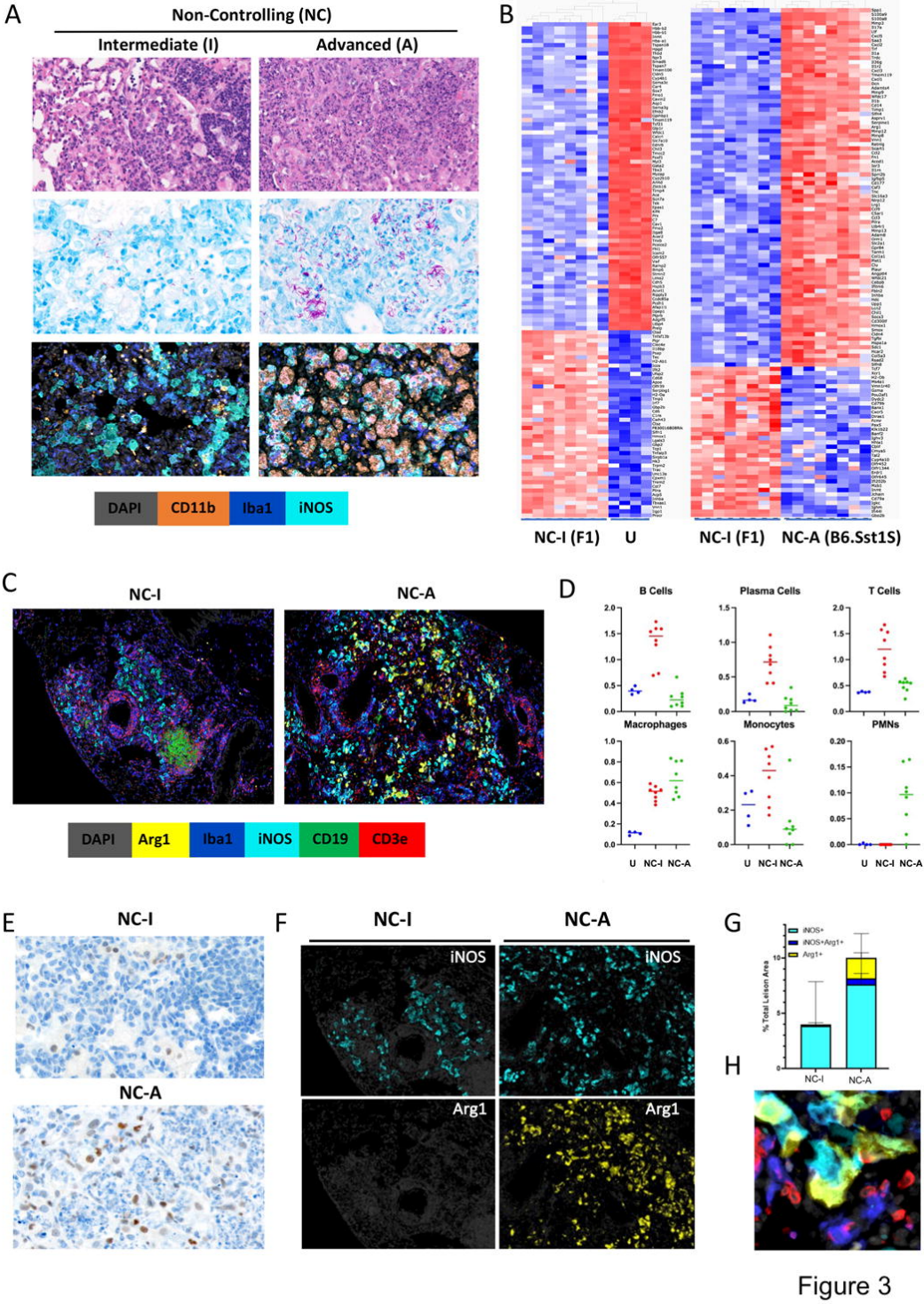
A
Non-Controlling (NC)
Intermediate (I)
Advanced (A)
DAPI
CD11b
Iba1
iNOS
B
NC-I (F1)
U
NC-I (F1)
NC-A (B6.Sst1S)
C
NC-I
NC-A
DAPI
Arg1
Iba1
iNOS
CD19
CD3e
D
B Cells
Plasma Cells
T Cells
Macrophages
Monocytes
PMNs
U
NC-I
NC-A
E
NC-I
NC-A
F
NC-I
NC-A
iNOS
iNOS
Arg1
Arg1
G
iNOS+
iNOS+Arg1+
Arg1+
% Total Lesion Area
NC-I
NC-A
H

Figure 3

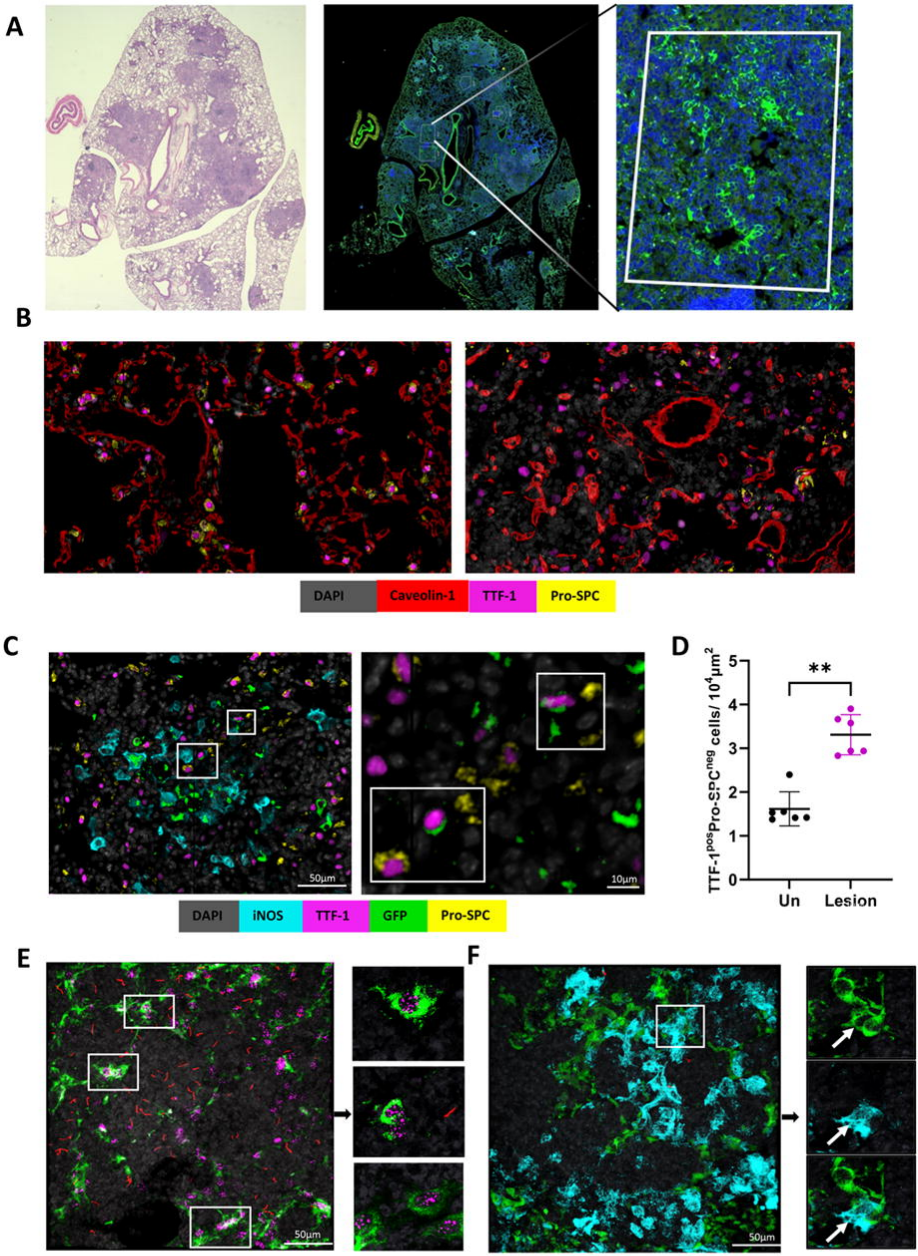
A
B
DAPI
Caveolin-1
TTF-1
Pro-SPC
C
50µm
10µm
DAPI
iNOS
TTF-1
GFP
Pro-SPC
D
**
TTF-1posPro-SPCneg cells/ 10⁴µm²
0
1
2
3
4
5
Un
Lesion
E
50µm
DAPI
TTF-1
YFP
Mtb
F
50µm
DAPI
iNOS
YFP
Mtb

Figure 4

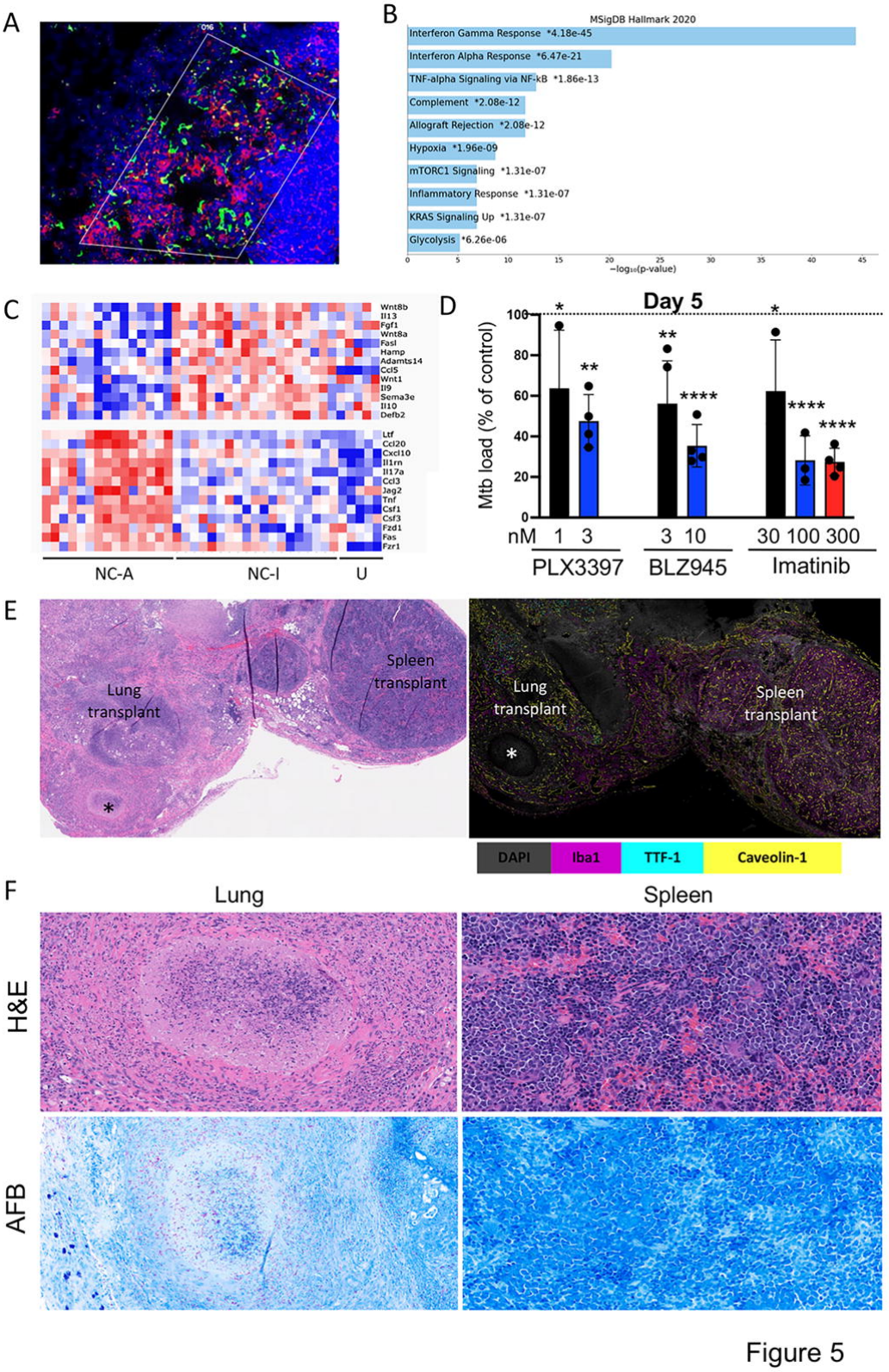
A
B
MSigDB Hallmark 2020
Interferon Gamma Response *4.18e-45
Interferon Alpha Response *6.47e-21
TNF-alpha Signaling via NF-kB *1.86e-13
Complement *2.08e-12
Allograft Rejection *2.08e-12
Hypoxia *1.96e-09
mTORC1 Signaling *1.31e-07
Inflammatory Response *1.31e-07
KRAS Signaling Up *1.31e-07
Glycolysis *6.26e-06
0 5 10 15 20 25 30 35 40 45
−log10(p-value)
C
Wnt8b
Il13
Fgf1
Wnt8a
Fasl
Hamp
Adamts14
Ccl5
Wnt1
Il9
Sema3e
Il10
Defb2
Ltf
Ccl20
Cxcl10
Il1rn
Il17a
Ccl3
Jag2
Tnf
Csf1
Csf3
Fzd1
Fas
Fzr1
NC-A
NC-I
U
D
Day 5
Mtb load (% of control)
100
80
60
40
20
0
nM 1 3 3 10 30 100 300
PLX3397
BLZ945
Imatinib
E
Lung transplant
Spleen transplant
Lung transplant
Spleen transplant
DAPI
Iba1
TTF-1
Caveolin-1
F
Lung
Spleen
H&E
AFB

Figure 5